

Single-scattering properties of ellipsoidal dust aerosols constrained by measured dust shape distributions

Yue Huang^{1,†} (ORCID: 0000-0002-7818-8432)

5 Jasper F. Kok¹ (ORCID: 0000-0003-0464-8325)

Masanori Saito² (ORCID: 0000-0001-5188-7471)

Olga Muñoz³ (ORCID: 0000-0002-5138-3932)

¹Department of Atmospheric and Oceanic Sciences, University of California, Los Angeles, CA 90095, USA

²Department of Atmospheric Sciences, Texas A&M University, College Station, TX 77843, USA

10 ³Instituto de Astrofísica de Andalucía (IAA-CSIC), Granada 18008, Spain

[†]Now at the Earth Institute, Columbia University, New York, NY 10025, USA, and NASA Goddard Institute for Space Studies (GISS), New York, NY 10025, USA

15 *Correspondence to:* Yue Huang (hyue3@yahoo.comh3456@columbia.edu)

Abstract. Most global aerosol models approximate dust as spherical particles, whereas most remote sensing retrieval algorithms approximate dust as spheroidal particles with a shape distribution that conflicts with measurements. These inconsistent and inaccurate shape assumptions generate biases in dust single-scattering properties. Here, we obtain dust single-scattering properties by approximating dust as tri-axial ellipsoidal particles with observationally constrained shape distributions. We find that, relative to the ellipsoidal dust optics obtained here, the spherical dust optics used in most aerosol models underestimate dust single-scattering albedo, mass extinction efficiency, and asymmetry parameter for almost all dust sizes in both the shortwave and longwave spectra. We further find that the ellipsoidal dust optics are in substantially better agreement with observations of the scattering matrix and linear depolarization ratio than the spheroidal dust optics used in most retrieval algorithms. However, relative to observations, the ellipsoidal dust optics overestimate the lidar ratio by underestimating the backscattering intensity by a factor of ~ 2 . This occurs largely because the computational method used to simulate ellipsoidal dust optics (i.e., the improved geometric optics method) underestimates the backscattering intensity by a factor of ~ 2 relative to other computational methods (e.g., the physical geometric optics method). We conclude that the ellipsoidal dust optics with observationally constrained shape distributions can help improve global aerosol models and possibly remote sensing retrieval algorithms that do not use the backscattering signal.

30

1 Introduction

Desert dust aerosols are a key atmospheric component (Mahowald et al., 2014; Kok et al., 2021a; 2021b; Adebiyi et al., 2023). Dust impacts the Earth system by modifying the radiation budget (Ito et al., 2021; Kok et al., 2023), hydrological cycle (Miller et al., 2004; 2006), cloud microphysics (Kiselev et al., 2017), and ocean biogeochemistry (Yu et al., 2015; Ito et al., 2019). Furthermore, dust impacts anthropogenic activities by degrading air quality and visibility (Mahowald et al., 2007; Huang et al., 2019) and harming human health (Giannadaki et al., 2014). To accurately estimate these dust impacts, global aerosol models and retrieval algorithms of passive and active remote sensing products need accurate dust single-scattering properties (Dubovik et al., 2006; Winker et al., 2007; Ansmann et al., 2012; Gliß et al., 2021).

Dust single-scattering properties highly depend on dust shape (Bi et al., 2009; 2010; Lindqvist et al., 2014; Nousianien and Kandler, 2015; Lin et al., 2018; Saito et al., 2021; Saito and Yang, 2021; Kong et al., 2022), but global aerosol models and remote sensing retrieval algorithms use inconsistent and inaccurate dust shape quantifications (Fig. 1). Specifically, almost all global aerosol models approximate dust as spherical particles (Fig. 1a; Gliß et al., 2021), whereas most retrieval algorithms approximate dust as spheroidal particles (Figs. 1b and 1c) and use the length-to-height ratio to quantify dust asphericity (Dubovik et al., 2006; Hsu et al., 2019). By assuming a spherical or spheroidal dust shape, aerosol models and retrieval algorithms equate at least two of three dust perpendicular axes. However, a recent study that compiled dozens of *in situ* measurements of dust shape worldwide found that the three perpendicular axes differ substantially for most dust particles and thus that the tri-axial ellipsoidal shape assumption (Fig. 1d) is more realistic for dust aerosols (Huang et al., 2020). In addition, relative to the compiled observations, aerosol models and retrieval algorithms substantially underestimate dust asphericity (Fig. 1e). These problematic dust shape assumptions of aerosol models and retrieval algorithms generate biases in dust single-scattering properties that further propagate into the estimated dust impacts.

To facilitate accounting for more realistic dust shape in aerosol models and retrieval algorithms, here we obtain dust single-scattering properties by approximating dust as tri-axial ellipsoidal particles with observationally constrained shape distributions (Sections 2). In Section 2, we then compare the obtained ellipsoidal dust optics with the spherical dust optics used in most aerosol models and the spheroidal dust optics used in most retrieval algorithms; these three optics simulations are validated against laboratory and field observations of dust optics. In Section 3, our results show that the ellipsoidal dust optics agree with observations substantially better than the spherical and spheroidal dust optics. Thus, the ellipsoidal dust optics with observationally constrained shape distributions can help improve aerosol models and retrieval algorithms.

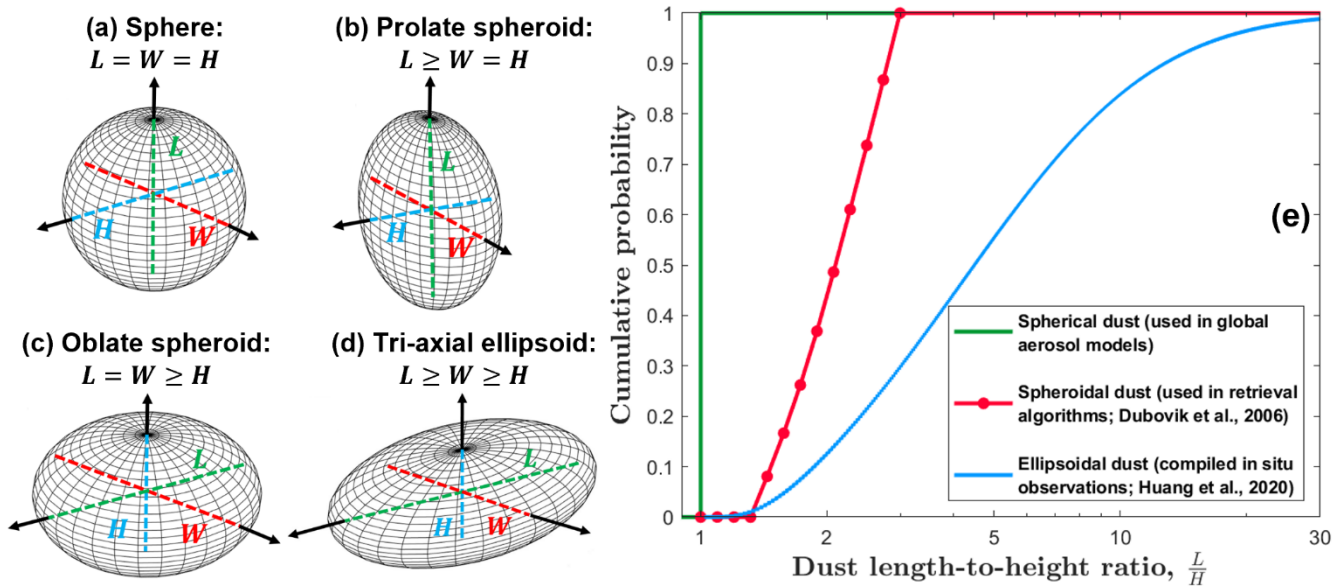


Figure 1. Global aerosol models and remote sensing retrieval algorithms use inconsistent and inaccurate dust shape quantifications. Most aerosol models approximate dust as (a) spherical particles whose three perpendicular axes (i.e., dust length L , width W , and height H) are equal (Gliß et al., 2021). Most retrieval algorithms approximate dust as spheroidal particles with an equal presence of (b) prolate spheroid and (c) oblate spheroid at the same length-to-height ratio (Dubovik et al., 2006). A compilation of dust shape measurements found that the three perpendicular axes differ substantially for most dust particles and thus that approximating dust as tri-axial ellipsoids (d) is more realistic (Huang et al., 2020). Panel (e) compares the cumulative probability distributions of the dust length-to-height ratio used in most aerosol models (in green) and retrieval algorithms (in red) and obtained from a measurement compilation (in blue; see Section 2.2). The red dots in panel (e) denote the 13 shape bins used in the AERONET retrieval algorithm (Dubovik et al., 2006; Giles et al., 2019). AERONET chose its dust shape distribution as the one that resulted in the best fit between the simulated scattering matrix and laboratory-measured scattering matrix of a sample of crushed feldspar rocks (see Section 2.3). However, this shape distribution conflicts with measurements of dust shape and is substantially less aspherical than natural dust aerosols. This optimized dust shape distribution is widely adopted in most other retrieval

algorithms (e.g., MODIS Deep Blue; Hsu et al., 2019). As such, aerosol models and retrieval algorithms substantially underestimate the dust length-to-height ratio relative to observations.

75

2 Methods

This section presents our methodology for obtaining and evaluating the single-scattering properties of tri-axial ellipsoidal dust aerosols constrained by measured dust shape distributions. In Section 2.1, we first introduce the definitions of single-scattering properties used in global aerosol models and remote sensing retrieval algorithms. Then, in Section 2.2, we 80 obtain the single-scattering properties of ellipsoidal dust ensembles accounting for observational constraints on dust shape. In Section 2.3, we introduce the laboratory and field observations used as the ground truth to evaluate our obtained ellipsoidal dust optics. This section also introduces the spherical and spheroidal dust optics used in most aerosol models and retrieval algorithms. By comparing the spherical, spheroidal, and ellipsoidal dust optics against observations, we can test our hypothesis that ellipsoidal dust optics constrained by measured dust shape distributions are more realistic than the spherical and spheroidal 85 dust optics.

2.1 Definitions of single-scattering properties

Single-scattering properties quantify how aerosols modify incident light after one instance of elastic scattering (Liou, 2002). Remote sensing retrieval algorithms and global aerosol models retrieve dust distributions and estimate dust impacts 90 using seven key single-scattering properties, namely phase function, asymmetry factor, extinction efficiency, mass extinction efficiency, single-scattering albedo, linear depolarization ratio, and lidar ratio. We present the definitions of these single-scattering properties in detail below.

The modification of the incident light by aerosol scattering is quantified by the scattering cross section and the 95 scattering matrix. The scattering cross section C_{sca} (unit: m^2) quantifies the total amount of light scattered by the aerosol particle. The 4×4 scattering matrix $P_{4 \times 4}$ (unitless) (also referred to as the Mueller matrix or the phase matrix) quantifies the angular modification of light by aerosol scattering (Liou, 2002; Mishchenko and Yurkin, 2017). Specifically, for an incident light beam (with intensity I_i , linear polarization components Q_i and U_i , and circular polarization component V_i), the scattered 100 light beam (with intensity I_s , linear polarization components Q_s and U_s , and circular polarization component V_s) after one single-scattering event with a randomly-oriented aerosol particle is (Liou, 2002),

$$\begin{bmatrix} I_s \\ Q_s \\ U_s \\ V_s \end{bmatrix} = \frac{C_{sca}}{4\pi s^2} \begin{bmatrix} P_{11} & P_{12} & 0 & 0 \\ P_{12} & P_{22} & 0 & 0 \\ 0 & 0 & P_{33} & P_{34} \\ 0 & 0 & -P_{34} & P_{44} \end{bmatrix} \begin{bmatrix} I_i \\ Q_i \\ U_i \\ V_i \end{bmatrix}, \quad (1)$$

where s (unit: m) is the distance between the light detector and the scatterer (i.e., the aerosol particle) and the 4×4 scattering matrix $P_{4 \times 4}$ has six non-zero independent elements for randomly-oriented aerosols (Mishchenko et al., 2002; Hovenier et al., 2004; Mishchenko and Yurkin, 2017). Among the six independent elements, the so-called phase function $P_{11}(\theta)$ describes the angular change in light intensity, and the other five elements describe the angular change in light polarization. The phase 105 function is normalized such that P_{11} integrated against the scattering angle θ and the azimuth angle ϕ yields 4π (Liou, 2002),

$$\int_0^{2\pi} \int_0^\pi P_{11}(\theta) \sin(\theta) d\theta d\phi = 4\pi. \quad (2)$$

The phase function is used in remote sensing retrieval algorithms to account for the angular distribution of aerosol-scattered radiation, whereas global aerosol models instead use the asymmetry factor to minimize computational costs. The asymmetry 110 factor g (unitless) is,

$$g = \frac{1}{2} \int_0^\pi P_{11} \sin(\theta) \cos(\theta) d\theta, \quad (3)$$

where g is in between -1 and 1 , $g = 0$ when the radiation is scattered isotropically, and g increases (decreases) with the increasing amount of light scattered into the forward (backward) hemisphere within $0^\circ < \theta < 90^\circ$ ($90^\circ < \theta < 180^\circ$) (Liou, 2002).

115 The other five elements of the scattering matrix quantify how the intensity and polarization of the outgoing light beam depends on the scattering angle and the polarization of the incoming light beam. Specifically, $-\frac{P_{12}(\theta)}{P_{11}(\theta)}$ quantifies the degree of linear polarization of the scattered light for the unpolarized component of the incident light, $1 - \frac{P_{22}(\theta)}{P_{11}(\theta)}$ quantifies the depolarization of the scattered light for the linear polarized component of the incident light, and $P_{33}(\theta)$, $P_{34}(\theta)$, and $P_{44}(\theta)$ quantify the modification on the circular polarization components by aerosol scattering (Liou, 2002; Nousiainen and Kandler, 2015; Mishchenko and Yurkin, 2017). These circular polarization components are rarely used in the current generation of 120 remote sensing products. Active remote sensing products (e.g., airborne and ground-based lidars) widely use the linear depolarization ratio δ (unitless) to distinguish dust aerosols from the other aerosol types. δ quantifies the depolarization of the backscattered light for the linear polarized component of the incident light as (Mishchenko and Hovenier, 1995; Winker et al., 2007; Ansmann et al., 2012; Nousiainen and Kandler, 2015),

$$\delta = \frac{P_{11}(\pi) - P_{22}(\pi)}{P_{11}(\pi) + P_{22}(\pi)} \quad (4).$$

125

In addition to aerosol scattering, aerosols can also modify the incident light by aerosol absorption, with the sum of scattering and absorption equalling the light extinction by aerosols. In analogy to the scattering cross section, the absorption and extinction cross sections C_{abs} (unit: m^2) and C_{ext} (unit: m^2) respectively quantify the total amount of light absorbed and extinguished by the aerosol particle. These three cross sections depend on the physical size of the aerosol particle as

$$130 \quad C_{sca/abs/ext} = Q_{sca/abs/ext} \cdot A, \quad (5)$$

where Q_{sca} , Q_{abs} , and Q_{ext} (unitless) are respectively the scattering, absorption, and extinction efficiencies that quantify a particle's ability to scatter, absorb, and extinguish light relative to its projected surface area A (unit: m^2) (Liou, 2002). In addition to the extinction efficiency, global aerosol models use the mass extinction efficiency MEE (unit: $m^2 kg^{-1}$) to quantify the light extinguished by aerosols per unit mass loading as (Kok et al., 2017),

$$135 \quad MEE = Q_{ext} \cdot \frac{A}{M}, \quad (6)$$

where M is the mass of the aerosol particle (unit: kg). To quantify the contribution of light scattering to light extinction by aerosols, global aerosol models use the single-scattering albedo SSA (unitless) as,

$$SSA = \frac{C_{sca}}{C_{ext}}, \quad (7)$$

which is in between 0 and 1 (Liou, 2002). Finally, remote sensing products widely use the lidar ratio S (unit: sr) to quantify 140 the ratio of extinct light to backscattered light (Liou, 2002; Dubovik et al., 2006; Nousiainen and Kandler, 2015) defined as

$$S = \frac{4\pi}{SSA \cdot P_{11}(\pi)}, \quad (8).$$

145 These seven key single-scattering properties depend on dust microphysical properties, including dust shape, size, and mineralogy composition. A range of studies have investigated the impacts of biases in dust size and refractive index on dust single-scattering properties (e.g., Formenti et al., 2011; Kok et al., 2017; Di Biagio et al., 2017; 2019; 2020; Swet et al., 2020; Klose et al., 2021; Li et al., 2021; 2022; Meng et al., 2022; González-Flórez et al., 2022), but fewer studies have focused on the impact of bias in dust shape. The studies that did consider dust asphericity (e.g., Dubovik et al., 2006; Colarco et al., 2014) used dust shape approximations that deviate from observations (Fig. 1) to obtain dust single-scattering properties. To help

150 quantify the biases in dust single-scattering properties due to dust shape, we ~~for the first time (to our knowledge)~~ account for the observational constraints on dust shape in obtaining dust single-scattering properties (Section 2.2).

2.2 Ellipsoidal dust optics with observationally constrained shape distributions

155 In this section, we first introduce two shape descriptors and their probability distributions from measurement compilation. We use these two probability distributions to quantify the asphericity of dust aerosols, approximating dust as tri-axial ellipsoidal particles. Second, we introduce an extensive database containing shape-resolved single-scattering properties of ellipsoidal dust aerosols. Finally, we obtain the single-scattering properties of ellipsoidal dust ensembles by combining the shape-resolved single-scattering properties database with the two probability distributions of dust shape.

160 Dozens of *in situ* measurements across the world have used the length-to-width ratio ($LWR = \frac{L}{W}$; see Fig. 1; ~~also~~ commonly referred to as the aspect ratio) and the height-to-width ratio ($HWR = \frac{H}{W}$; see Fig. 1) to determine the shape of hundreds of thousands of individual dust particles. These measurements were compiled by Huang et al. (2020) and showed that both HWR and the deviation of LWR from unity (i.e., $LWR - 1$) follow a lognormal distribution as (e.g., Okada et al., 2001; Reid et al., 2003; Kandler et al., 2007; 2009; 2011; Sakai et al., 2010)

$$165 f(LWR) = \frac{1}{\sqrt{2\pi} \cdot (LWR - 1) \cdot \sigma_L} \exp \left[-\frac{1}{2} \left(\frac{\ln(LWR - 1) - \ln(\bar{\varepsilon}_L - 1)}{\sigma_L} \right)^2 \right], \quad (9)$$

$$f(HWR) = \frac{1}{\sqrt{2\pi} \cdot HWR \cdot \sigma_H} \exp \left[-\frac{1}{2} \left(\frac{\ln(HWR) - \ln(\bar{\varepsilon}_H)}{\sigma_H} \right)^2 \right], \quad (10)$$

170 where $\bar{\varepsilon}_L$ and $\bar{\varepsilon}_H$ are respectively the medians of LWR and HWR , and σ_L and σ_H are respectively the geometric standard deviations of $LWR - 1$ and HWR . In addition, Huang et al. (2020) found that both LWR and HWR are insensitive to dust particle diameter, and that the regional differences in LWR and HWR are modest. In the present study, we thus take $\bar{\varepsilon}_L = 1.70 \pm 0.03$, $\bar{\varepsilon}_H = 0.40 \pm 0.07$, $\sigma_L = 0.70 \pm 0.02$, and $\sigma_H = 0.73 \pm 0.09$ after the global averages compiled by Huang et al. (2020). Using these two globally representative shape distributions, we approximate dust as tri-axial ellipsoidal particles with smooth surfaces and neglect the smaller-scale surface texture (such as sharp corners and surface roughness; Kalashnikova and Sokolik, 2004; Kemppinen et al., 2015; Saito et al., 2021; Saito and Yang, 2021; see Section 4.3 for a discussion of the impacts of these simplifications).

175 We seek to combine the two globally representative dust shape distributions (Eqs. 9 and 10) with an extensive database containing single-scattering properties of ellipsoidal dust aerosols (Meng et al., 2010). This database combined four computational methods (~~Lorenz Mie theory, T matrix method, discrete dipole approximation, and an improved geometric optics method~~) to compute the single-scattering properties: Lorenz-Mie theory was used for spherical particles with size parameter x of 0.025 – 1000, the T-matrix method was used for particles with x of 0.025 – 40, the discrete dipole approximation was used for x of 0.025 – 40, and the improved geometric optics method was used for x of 10 – 1000 (see Table 2 of Meng et al., 2010). At overlapping size parameters, results from different methods were averaged. These four methods together cover the size parameter range from Rayleigh to the geometric optics regimes. This extensive database contains the extinction efficiency $Q_{ext}(n, k, x, LWR, HWR)$, the single-scattering albedo $SSA(n, k, x, LWR, HWR)$, the asymmetry factor $g(n, k, x, LWR, HWR)$, and the six independent elements of the 4×4 scattering matrix $P_{4 \times 4}(n, k, x, LWR, HWR, \theta)$. These pre-calculated optics are resolved by the real (n) and imaginary (k) parts of dust refractive index, the size parameter (x), the length-to-width ratio and height-to-width ratio of the ellipsoidal dust particle (LWR and HWR), and the scattering angle (θ). We direct interested readers to Tables 1 and 2 of Meng et al. (2010) for the ranges of n , k , x , LWR , and HWR of the database.

190 We combined the shape-resolved optics database (Meng et al., 2010) with the two globally representative probability distributions of dust shape (Eqs. 9 and 10) to obtain the single-scattering properties of ensembles of ellipsoidal dust particles. That is, at a given dust volume-equivalent diameter, the obtained optics are ensemble averages of the single-scattering

properties of 121 particle shapes (i.e., 11 values of *LWR* and 11 values of *HWR*; Meng et al., 2010); the weighting factor assigned to each particle shape, $f_w(LWR, HWR)$, was determined by the two lognormal distributions of *LWR* and *HWR* (Eqs. 9 and 10). As such, at a given dust refractive index (n and k), light wavelength (λ), and dust volume-equivalent diameter (D), we obtain the extinction efficiency, mass extinction efficiency, single-scattering albedo, asymmetry factor, scattering matrix, linear depolarization ratio, and lidar ratio of ellipsoidal dust ensembles as (Liou, 2002; Grainger, 2020),

$$\hat{Q}_{ext}(n, k, \lambda, D) = \frac{4}{\pi D^2} \hat{\beta}_{ext}(n, k, \lambda, D), \quad (11)$$

$$\overline{MEE}(n, k, \lambda, D) = \hat{Q}_{ext}(n, k, \lambda, D) \cdot \frac{3}{2\rho D}, \quad (12)$$

$$\widehat{SSA}(n, k, \lambda, D) = \frac{\hat{\beta}_{sca}(n, k, \lambda, D)}{\hat{\beta}_{ext}(n, k, \lambda, D)}, \quad (13)$$

$$\hat{g}(n, k, \lambda, D) = \frac{1}{\hat{\beta}_{sca}(n, k, \lambda, D)} \sum_{w=1}^{121} \left[\frac{\pi D^2}{4} \cdot SA_w(LWR, HWR) \cdot Q_{ext}(n, k, \lambda, D, LWR, HWR) \cdot SSA(n, k, \lambda, D, LWR, HWR) \cdot g(n, k, \lambda, D, LWR, HWR) \cdot f_w(LWR, HWR) \right], \quad (14)$$

$$\widehat{P}_{ij}(n, k, \lambda, D, \theta) = \frac{1}{\hat{\beta}_{sca}(n, k, \lambda, D)} \sum_{w=1}^{121} \left[\frac{\pi D^2}{4} \cdot SA_w(LWR, HWR) \cdot Q_{ext}(n, k, \lambda, D, LWR, HWR) \cdot SSA(n, k, \lambda, D, LWR, HWR) \cdot P_{ij}(n, k, \lambda, D, LWR, HWR, \theta) \cdot f_w(LWR, HWR) \right], \quad (15)$$

$$\delta(n, k, \lambda, D) = \frac{\widehat{P}_{11}(n, k, \lambda, D, 180^\circ) - \widehat{P}_{22}(n, k, \lambda, D, 180^\circ)}{\widehat{P}_{11}(n, k, \lambda, D, 180^\circ) + \widehat{P}_{22}(n, k, \lambda, D, 180^\circ)}, \quad (16)$$

$$\hat{S}(n, k, \lambda, D) = \frac{4\pi}{\widehat{SSA}(n, k, \lambda, D) \widehat{P}_{11}(n, k, \lambda, D, 180^\circ)}, \quad (17)$$

$$\hat{\beta}_{ext}(n, k, \lambda, D) = \sum_{w=1}^{121} \left[\frac{\pi D^2}{4} \cdot SA_w(LWR, HWR) \cdot Q_{ext}(n, k, \lambda, D, LWR, HWR) \cdot f_w(LWR, HWR) \right], \quad (18)$$

$$\hat{\beta}_{sca}(n, k, \lambda, D) = \sum_{w=1}^{121} \left[\frac{\pi D^2}{4} \cdot SA_w(LWR, HWR) \cdot Q_{ext}(n, k, \lambda, D, LWR, HWR) \cdot SSA(n, k, \lambda, D, LWR, HWR) \cdot f_w(LWR, HWR) \right] \quad (19)$$

where $ij = 11, 12, 22, 33, 34$, and 44 denote the six independent elements of the 4×4 scattering matrix, $\hat{\beta}_{ext}$ and $\hat{\beta}_{sca}$ are respectively the bulk volume extinction and scattering coefficients, $f_w(LWR, HWR)$ is the normalized weighting factor of the w^{th} particle shape among the total 121 particle shapes, such that the sum of the 121 weighting factors yields unity. To obtain

these weighting factors were calculated, we used Monte Carlo sampling to randomly generate a large number (10^8) of volume-equivalent ellipsoidal dust particles from the two lognormal distributions of *LWR* and *HWR* (Eqs. 9 and 10). Note that the upper limits of *LWR* and *HWR* are both 3.3 in the Meng et al. (2010) database, whereas observations find dust particles can be more aspherical (Huang et al., 2020). For a dust particle with a *LWR* (or *HWR*) larger than 3.3, we assume its *LWR* (or *HWR*) is 3.3. Future database development to include these highly aspherical shapes is highly recommended.

$SA_w(LWR, HWR)$ is the ratio between the projected surface area of an ellipsoidal dust particle and the projected surface area of the volume-equivalent spherical dust particle, with the ellipsoidal dust particle having the w^{th} particle shape among the total 121 particle shapes. We use this conversion factor to bridge the gap between two different definitions of extinction efficiency. Meng et al. (2010) database calculated the extinction efficiency with regards to the projected surface area of the ellipsoidal particle, whereas global aerosol models use the extinction efficiency with regards to the projected surface area of the volume-equivalent sphere (Kok et al., 2017). Since an ellipsoidal particle has a larger surface area than its volume-equivalent spherical particle, $SA_w(LWR, HWR)$ always exceeds unity. That is, although the 121 extinction efficiencies of the 121 shapes in Meng et al. (2010) approach an asymptotic value of 2 at large particle sizes (based on optical theorem of extinction; see Eq. 3.3.27 of Liou, 2002), the output extinction efficiency, $\hat{Q}_{ext}(n, k, \lambda, D)$, can be larger than 2 at large particle sizes (see Fig. 2) since they are corrected to account for $SA_w(LWR, HWR)$.

Using the equations above, we obtain the single-scattering properties of ellipsoidal dust ensembles constrained by measured dust shape distributions. The obtained ellipsoidal dust optics for use in global aerosol models (\overline{MEE} , \widehat{SSA} , and \hat{g}) are in a 4-dimensional (4-D) space, resolved by the real and imaginary parts of dust refractive index, light wavelength, and dust volume-equivalent diameter. The obtained ellipsoidal dust optics for use by remote sensing retrievals are either in a 4-D space (for δ and \hat{S}) or in a 5-D space (for \widehat{P}_{ij}) with an extra dimension as the scattering angle. We provided a publicly accessible

repository with the look-up tables containing the ellipsoidal dust optics in these 4-D and 5-D spaces (see Code/Data availability).

235

2.3 Observations to evaluate the simulated dust optics

We treat the observations of dust optics as the ground truth to evaluate our obtained ellipsoidal dust optics (Section 2.2) and the spherical and spheroidal dust optics used in previous studies. In this section, we first introduce laboratory 240 observations of the scattering matrix and field observations of the linear depolarization ratio and lidar ratio. Second, we introduce the spherical and spheroidal dust optics used in most global aerosol models and remote sensing retrieval algorithms. Third, we integrate the size-resolved spherical, spheroidal, and ellipsoidal dust optics simulations over the dust particle size 245 distributions observed for the laboratory and field observations. This integration enables comparisons on an equal footing, since the three optics simulations are size-resolved, whereas the observations were obtained for a mixture of dust aerosols with various particle sizes. Finally, we calculate the root-mean square errors between the optics simulations and observations to quantify the performance of the three optics simulations.

The Amsterdam-Granada light scattering database (AGLSD; Muñoz et al., 2012) is publicly-accessible (see Code/Data availability) and has been widely regarded as the standard to evaluate dust optical models (e.g., Nousiainen and Vermeulen, 2003; Dubovik et al., 2006; Merikallio et al., 2011; Lindqvist et al., 2014; Saito and Yang, 2021). AGLSD contains 250 laboratory measurements of the scattering matrices at two visible wavelengths of tens of samples with simultaneous measurements of these samples' particle size distributions. Among these samples, we select two dust samples (i.e., newGobi and newSaharaOSN) and one mineral sample (i.e., feldspar) to evaluate the simulated dust optics for the following reasons. The two dust samples were collected respectively during an intense Gobi dust event reaching Beijing (China) in 2006 and an intense Saharan dust event reaching the Observatory of Sierra Nevada in Granada (Spain) in 2004 (Gómez Martín et al., 2021). 255 These two samples are deposited dust aerosols, which are different from the other mineral samples included in AGLSD that were either purchased from commercial sources or generated in the lab by grinding mineral rocks and are thus less accurate representations of dust aerosols (Muñoz et al., 2012; Gómez Martín et al., 2021). In addition to the two dust samples, we also select the mineral sample feldspar. Although the sample feldspar was generated from grinded feldspar rocks (Volten et al., 2001) and its representativeness for natural dust aerosols remains uncertain, we still select it because it is the only sample used 260 to constrain the retrieval algorithm of AERONET (Dubovik et al., 2006) as the newGobi and newSaharaOSN samples have only recently become available (Gómez Martín et al., 2021).

A range of field campaigns have measured the linear depolarization ratio and lidar ratio for Saharan and Asian dust aerosols. During these field campaigns, ground-based or aircraft-carried lidars measured the linear depolarization ratio and 265 lidar ratio of dust plumes at the three common lidar wavelengths of 355, 532, and 1064 nm. We combine the measurement compilations of Tesche et al. (2019) and Saito and Yang (2021) and a new measurement study published after 2021 (i.e., Haarig et al., 2022). This yields a total of six datasets of linear depolarization ratio and eight datasets of lidar ratio at three 270 wavelengths (Tesche et al., 2009; 2011; Groβ et al., 2011; 2015; Burton et al., 2015; Harrig et al., 2017; 2022; Hofer et al., 2020; Hu et al., 2020). We neglect the minor effects of dust multiple scattering and dust mixing with other aerosols on the observation results, as Tesche et al. (2019) and Saito and Yang (2021) did.

Regarding the optics simulations, most global aerosol models use spherical dust optics (Fig. 1a), and most remote 275 sensing retrieval algorithms use spheroidal dust optics (Figs. 1b and 1c) with a shape distribution that conflicts with observations. Aerosol models and retrieval algorithms use look-up tables containing pre-calculated dust optics to reduce the computational costs. The look-up table of most aerosol models was calculated by Lorenz-Mie theory (Liou, 2002). The most widely used look-up table of retrieval algorithms was calculated by Dubovik et al. (2006) using the following three steps. First, Dubovik et al. (2006) combined two computational methods (T-matrix method and geometric-optics-integral-equation method) to calculate the spheroidal dust optics resolved in a 5-D space (i.e., n , k , λ , D , and length-to-height ratio). Second, they used these 5-D optics to retrieve the probability distribution of length-to-height ratio that enables the best agreement with 280 the observed scattering matrix of AGLSD sample feldspar (see Fig. 13 of Dubovik et al., 2006). Finally, Dubovik et al. (2006)

integrated the 5-D optics over the retrieved distribution of length-to-height ratio to obtain the spheroidal dust optics in a 4-D space (i.e., n , k , λ , and D). Dubovik et al. (2006)'s look-up table containing these spheroidal dust optics in the 4-D space has been used in many retrieval algorithms (for example, AERONET and Deep Blue of MODIS; Hsu et al., 2019). That is, these remote sensing retrievals chose their dust shape distribution as the one that resulted in the best fit between the simulated scattering matrix and the observed scattering matrix of the AGLSD sample feldspar; however, this shape distribution conflicts with measurements of dust shape and is substantially less aspherical than natural dust aerosols (Fig. 1e; Kandler et al., 2007; 2009; 2011; Huang et al., 2020).

We use the observations of dust optics as the ground truth to evaluate the spherical, spheroidal, and ellipsoidal dust optics simulations. However, the three optics simulations are resolved by dust particle size and refractive index, whereas the observations were obtained for a mixture of dust aerosols with various sizes and mineral compositions. The AGLSD laboratory observations measured the samples' particle size distributions (PSD) but did not measure their refractive indices, whereas the field lidar observations did not measure the PSD or the refractive index of dust plumes. To enable comparisons between the optics simulations and observations on an equal footing, we make the following three assumptions about PSD and refractive index. First, for the three AGLSD samples (i.e., newGobi, newSaharaOSN, and feldspar), we assume the PSDs measured by AGLSD are accurate; for the dust plumes observed by field lidar observations across the world, we use the dust PSD obtained by Adebiyi and Kok (2020), who presented a globally representative PSD of atmospheric dust by leveraging aircraft observations and model simulations. Second, we set the cut-off diameter of all three optics simulations at 63 μm , because the PSDs of the two AGLSD samples (i.e., newGobi and newSaharaOSN) are coarser than the cut-off diameter of Dubovik et al. (2006)'s look-up table (i.e., 63 μm). Third, for the three AGLSD samples and dust plumes observed by field lidar observations, we take the dust refractive index as $1.53 \pm 0.03 - i * 10^{-2.75 \pm 0.25}$ covering the globally representative ranges in previous studies (i.e., summarized in Kok et al., 2017; Di Biagio et al., 2017; 2019). With the three assumptions above, we integrated the size-resolved scattering matrix of spherical, spheroidal, and ellipsoidal dust optics simulations, $\widehat{P}_{ij}(n, k, \lambda, D, \theta)$, over the number PSDs of the three AGLSD samples and Adebiyi and Kok (2020), $\frac{dN}{dlnD}$, as (Liou, 2002; Grainger, 2020),

$$305 \quad \widehat{P}_{ij}(n, k, \lambda, \theta) = \frac{1}{\int_{D_{min}}^{D_{max}} \frac{dN}{dlnD} dlnD} \cdot \int_{D_{min}}^{D_{max}} \left[\frac{\pi D^2}{4} \cdot \widehat{Q}_{ext}(n, k, \lambda, D) \cdot \widehat{SSA}(n, k, \lambda, D) \cdot \widehat{P}_{ij}(n, k, \lambda, D, \theta) \cdot \frac{dN}{dlnD} \right] dlnD \quad (20).$$

We then used the scattering matrix of bulk dust aerosols obtained from Eq. (20) to calculate the simulated linear depolarization ratio and lidar ratio of bulk dust aerosols as

$$\delta(n, k, \lambda) = \frac{\widehat{P}_{11}(n, k, \lambda, 180^\circ) - \widehat{P}_{22}(n, k, \lambda, 180^\circ)}{\widehat{P}_{11}(n, k, \lambda, 180^\circ) + \widehat{P}_{22}(n, k, \lambda, 180^\circ)}, \quad (21)$$

$$310 \quad \widehat{S}(n, k, \lambda) = \frac{4\pi}{\widehat{SSA}(n, k, \lambda) \cdot \widehat{P}_{11}(n, k, \lambda, 180^\circ)} \quad (22).$$

As such, we obtained the simulated optics of bulk spherical, spheroidal, and ellipsoidal dust aerosols for the range of the globally representative dust refractive index at the two AGLSD wavelengths and the three lidar wavelengths. These optics simulations can be compared with the optics observations to evaluate the performance of the three optics simulations.

We used the root-mean square error (RMSE) to quantify the agreement between the observed and simulated scattering matrix at forward-, side-, and back-scattering angles. Specifically, we first interpolate the simulated scattering matrix onto the same scattering angles used by the AGLSD observations. We then calculated the RMSE as (Merikallio et al., 2011; Lindqvist et al., 2014)

$$315 \quad RMSE = \sqrt{\frac{1}{N} \sum_{\theta_2}^{\theta_2} \left[\log_{10} \left(\frac{P_{ij,obs}(\theta)}{P_{11,obs}(30^\circ)} \right) - \log_{10} \left(\frac{P_{ij,sim}(\theta)}{P_{11,sim}(30^\circ)} \right) \right]^2}, ij = 11 \quad (23)$$

$$320 \quad RMSE = \sqrt{\frac{1}{N} \sum_{\theta_1}^{\theta_2} \left[\frac{P_{ij,obs}(\theta)}{P_{11,obs}(\theta)} - \frac{P_{ij,sim}(\theta)}{P_{11,sim}(\theta)} \right]^2}, ij = 12 \text{ and } 22 \quad (24)$$

where the RMSE of P_{11} is calculated in logarithmic space because P_{11} varies over several orders of magnitude, and N is the number of data points within the scattering angle range $[\theta_1, \theta_2]$. The scattering angle ranges are respectively $[5^\circ, 35^\circ]$ at the forward-scattering direction, $[75^\circ, 105^\circ]$ at the side-scattering direction, and $[143^\circ, 173^\circ]$ at the back-scattering direction. The AGLSD observed scattering matrix at $\theta < 5^\circ$ and $\theta > 173^\circ$ is not available due to technical difficulties in measuring at these

325 angles (Volten et al., 2001; Muñoz et al., 2012; Gómez Martín et al., 2021). We used Eqs. (23) and (24) to compare the RMSEs between the three optics simulations (i.e., spherical, spheroidal, and ellipsoidal dust optics) and the AGLSD observations of three samples (i.e., newGobi, newSaharaOSN, and feldspar) at two visible wavelengths.

3 Results

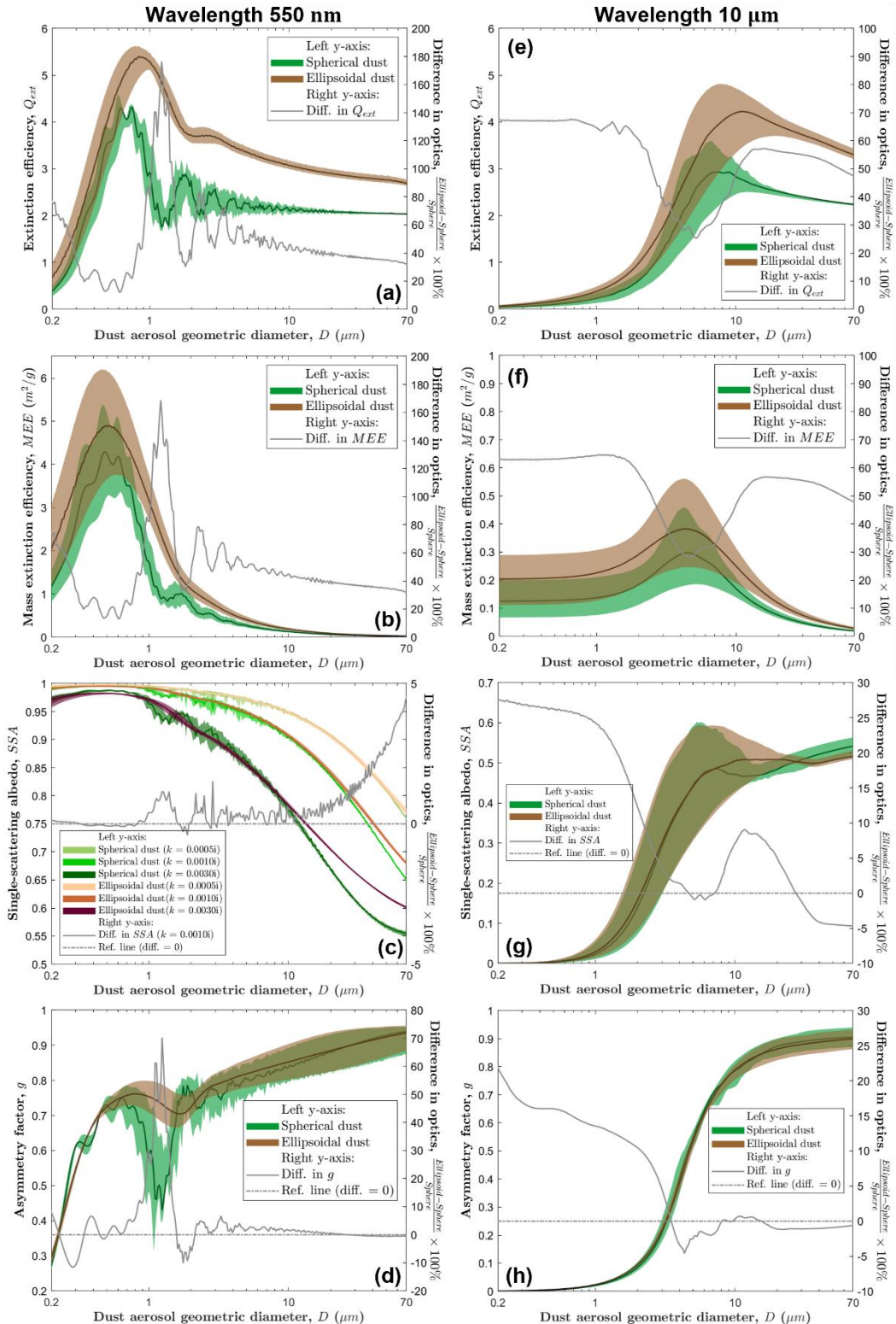
330 We obtained dust single-scattering properties by approximating dust as tri-axial ellipsoidal particles with observationally constrained shape distributions. We compared these ellipsoidal dust optics with the spherical dust optics used in most global aerosol models and spheroidal dust optics used in most remote sensing retrievals. These comparisons help quantify the biases in global aerosol models and remote sensing retrievals due to problematic dust shape approximations.

335 We find that, relative to ellipsoidal dust optics, the spherical dust optics used in most global aerosol models underestimate the four key dust single-scattering properties for almost all dust sizes in both the shortwave and longwave spectra. First, most aerosol models underestimate the extinction efficiency (Q_{ext}) and mass extinction efficiency (MEE) by 20% to 180% in the shortwave spectrum (Figs. 2a and 2b) and by 30% to 70% in the longwave spectrum (Figs. 2e and 2f). The peak magnitude difference between the two sets of optical properties occurs at dust sizes slightly larger than the wavelength in the shortwave spectrum: at $D = \sim 1 \mu\text{m}$, aerosol models underestimate Q_{ext} by ~ 3 and underestimate MEE by 340 $\sim 1 \text{ m}^2\text{g}^{-1}$. In the longwave spectrum, the peak magnitude difference occurs at dust sizes comparable to the wavelength: at $D = \sim 10 \mu\text{m}$, aerosol models underestimate Q_{ext} by ~ 1.5 and underestimate MEE by $\sim 0.1 \text{ m}^2\text{g}^{-1}$. Second, most aerosol models underestimate the single-scattering albedo (SSA) by up to 5% in the shortwave spectrum (Fig. 2c) and by up to 25% in the longwave spectrum (Fig. 2g). The magnitude difference between the two sets of optics in general increases with dust size and imaginary dust refractive index in both the shortwave and longwave spectra. Finally, most aerosol models slightly 345 underestimate the asymmetry factor (g) at most dust sizes (Figs. 2d and 2h), except at $D = \sim 1 \mu\text{m}$ in the shortwave spectrum where aerosol models underestimate g by up to 70% (Fig. 2d).

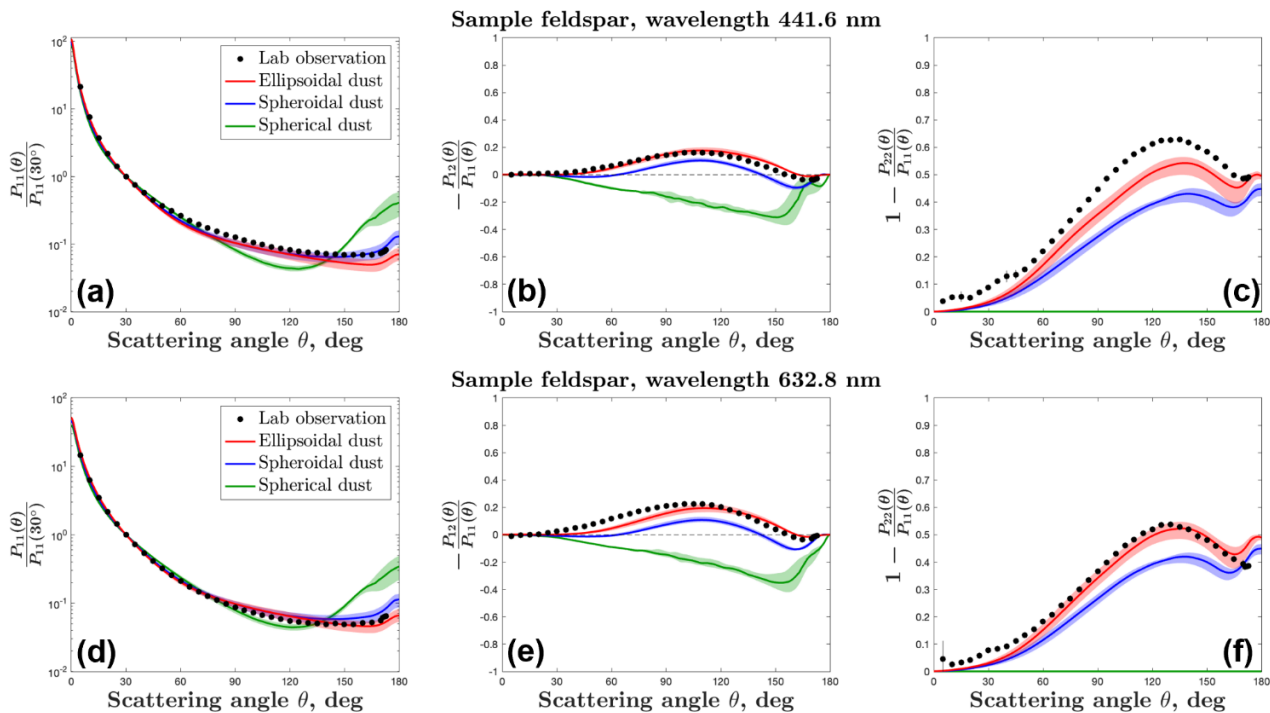
350 We further find that the ellipsoidal dust optics can reproduce the laboratory-measured phase function (i.e., P_{11}) and degree of linear polarization (i.e., $-\frac{P_{12}}{P_{11}}$) of AGLSD sample feldspar substantially better than the spherical and spheroidal dust optics (Fig. 3); however, it does not perform better than the spheroidal dust optics in reproducing the other two AGLSD samples (i.e., newGobi and newSaharaOSN; Figs. 4 and 5). Using the root-mean-square error (RMSE) to quantify the 355 disagreement between observation and simulation, the RMSEs between the laboratory measurements of feldspar optics and the ellipsoidal dust optics are the least at all scattering angles (Fig. 6). However, when comparing against the observations of newGobi and newSaharaOSN, the ellipsoidal dust optics almost always have larger RMSEs than the spheroidal dust optics (Fig. 6). Relative to all three AGLSD samples, the ellipsoidal dust optics underestimate the phase function at backscattering 360 angles (Figs. 3, 4, and 5), resulting in an overestimation in the estimated lidar ratio (S) (Fig. 7b; see Eq. (22) for the relationship between P_{11} and S). Compiled field observations of Saharan and Asian dust aerosols find that S is $\sim 50 \text{ sr}$ at the wavelengths of 355 nm and 532 nm and increases to $\sim 60 \text{ sr}$ at 1064 nm (Fig. 7b). The ellipsoidal dust optics overestimate S by a factor of 2 and 1.3 respectively at the two smaller and the largest wavelengths. The spheroidal dust optics can nicely reproduce S at 355 nm and 532 nm, but somewhat underestimate S at 1064 nm (Fig. 7b). The spherical dust optics underestimate S by more than a factor of ~ 3 at all wavelengths (Fig. 7b). For all three sets of optics, the magnitude difference between the observed and simulated S is consistent with the magnitude difference between the observed and simulated P_{11} at the scattering angle of 180° (Figs. 3, 4, and 5).

365 In addition, we find that the ellipsoidal dust optics can reproduce the laboratory-measured depolarization of incident polarized light (i.e., $1 - \frac{P_{22}}{P_{11}}$) substantially better than the spherical and spheroidal dust optics. The RMSEs between the laboratory observations of the three AGLSD samples and the ellipsoidal dust optics are the least at all scattering angles (Figs. 6c and 6f). The ellipsoidal dust optics have lower RMSEs than the spheroidal and spherical dust optics respectively by a factor of 1.5 and 2 at forward-scattering angles, by a factor of 2 and 3 at side-scattering angles, and by a factor of 2 and 4 at

370 backscattering angles (Figs. 6c and 6f). As a result of its excellent performance at backscattering angles, the ellipsoidal dust
375 optics can reproduce the field lidar observations of the linear depolarization ratio (δ) substantially better than the spherical and
spheroidal dust optics (Fig. 7a; see Eq. (21) for the relationship between $\frac{P_{22}}{P_{11}}$ and δ). Compiled field observations of Saharan
and Asian dust aerosols find that δ is ~ 0.25 at the wavelength of 355 nm, increases to ~ 0.3 at 532 nm, increases to ~ 0.36
375 at 710 nm, and then either stays constant or decreases to ~ 0.26 at 1064 nm (Fig. 7a). The ellipsoidal dust optics reproduce
both the magnitude and this wavelength dependency of the field observed δ . In contrast, the spheroidal dust optics predict an
incorrect magnitude and wavelength dependency of δ , and the spherical dust optics incorrectly predict that δ is always zero
because spherical dust particles do not depolarize incident light (see panels (c) and (f) of Figs. 3, 4, and 5).



380 **Figure 2. Single-scattering properties of spherical and tri-axial ellipsoidal dust aerosols in the shortwave and longwave**
 spectra. The left column includes (a) extinction efficiency Q_{ext} , (b) mass extinction efficiency MEE , (c) single-scattering
 albedo SSA , and (d) asymmetry factor g as a function of dust geometric diameter D at the wavelength of 550 nm. The right
 column includes (e) Q_{ext} , (f) MEE , (g) SSA , and (h) g as a function of D at the wavelength of 10 μm . In each plot, the left y-
 axis corresponds to the single-scattering properties of spherical (in green) and ellipsoidal dust aerosols (in brown); the central
 385 lines denote the medians, and the shaded ranges represent the 95% confidence intervals. The right y-axis corresponds to the
 difference in the median single-scattering properties of the two shape approximations (in grey). The uncertainties in spherical
 dust optics are due to uncertainties in the dust refractive index (see Section 2.3), and the uncertainties in ellipsoidal dust optics
 are due to uncertainties in the dust refractive index and dust shape distributions (see Sections 2.2 and 2.3). Panel (c) shows
 390 SSA at three different imaginary dust refractive indices (i.e., $k = 0.0005i$, $0.001i$, and $0.003i$) with the confidence intervals
 arising from uncertainties in the real dust refractive index and dust shape distributions; the grey line in panel (c) denotes the
 difference in the median SSA of the two shape approximations at $k = 0.001i$.



395 **Figure 3. Comparison of the laboratory-measured scattering matrix of AGLSD mineral sample feldspar against the**
 spherical, spheroidal, and ellipsoidal dust optics simulations at the wavelengths of 441.6 nm (top panels) and
 400 632.8 nm (bottom panels). For the three simulations, the central lines denote the medians, and the shaded ranges represent
 the 95% confidence intervals; these uncertainties are due to uncertainties in the dust refractive index and dust shape
 distributions (see Sections 2.2 and 2.3).

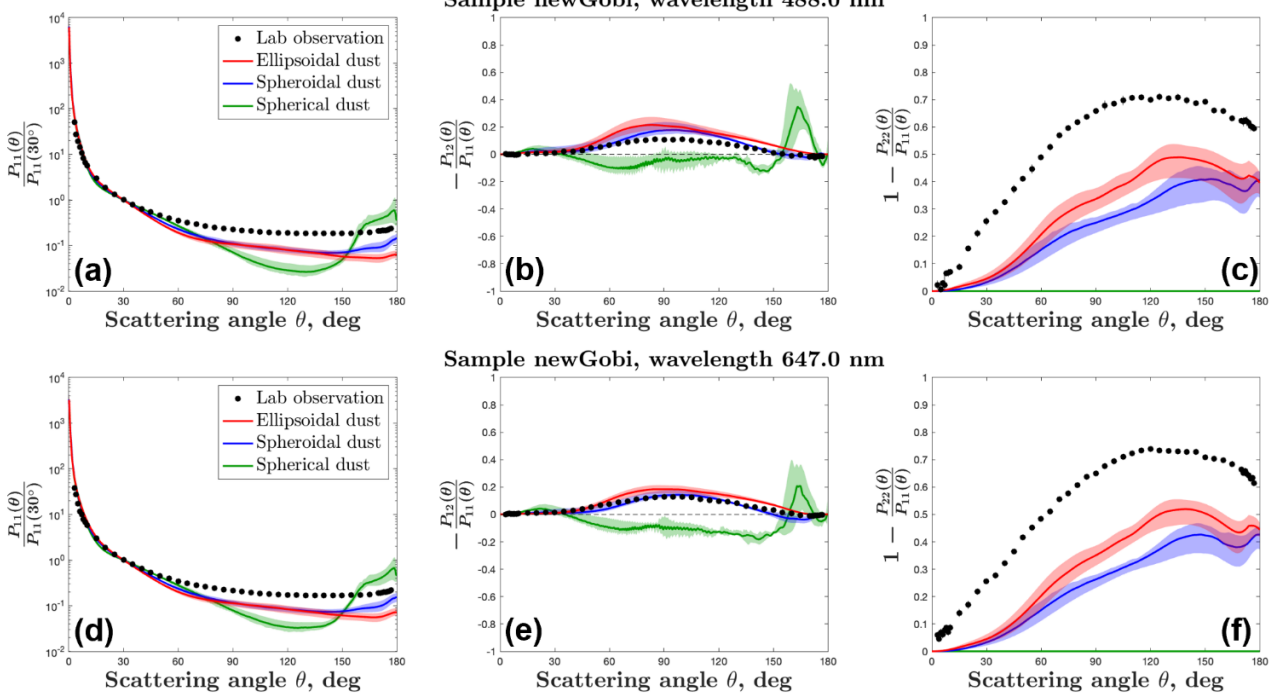


Figure 4. Same as figure 3, except for comparison of the laboratory-measured scattering matrix of AGLSD dust sample newGobi against the spherical, spheroidal, and ellipsoidal dust optics simulations at the wavelengths of 488.0 nm and 647.0 nm.

405

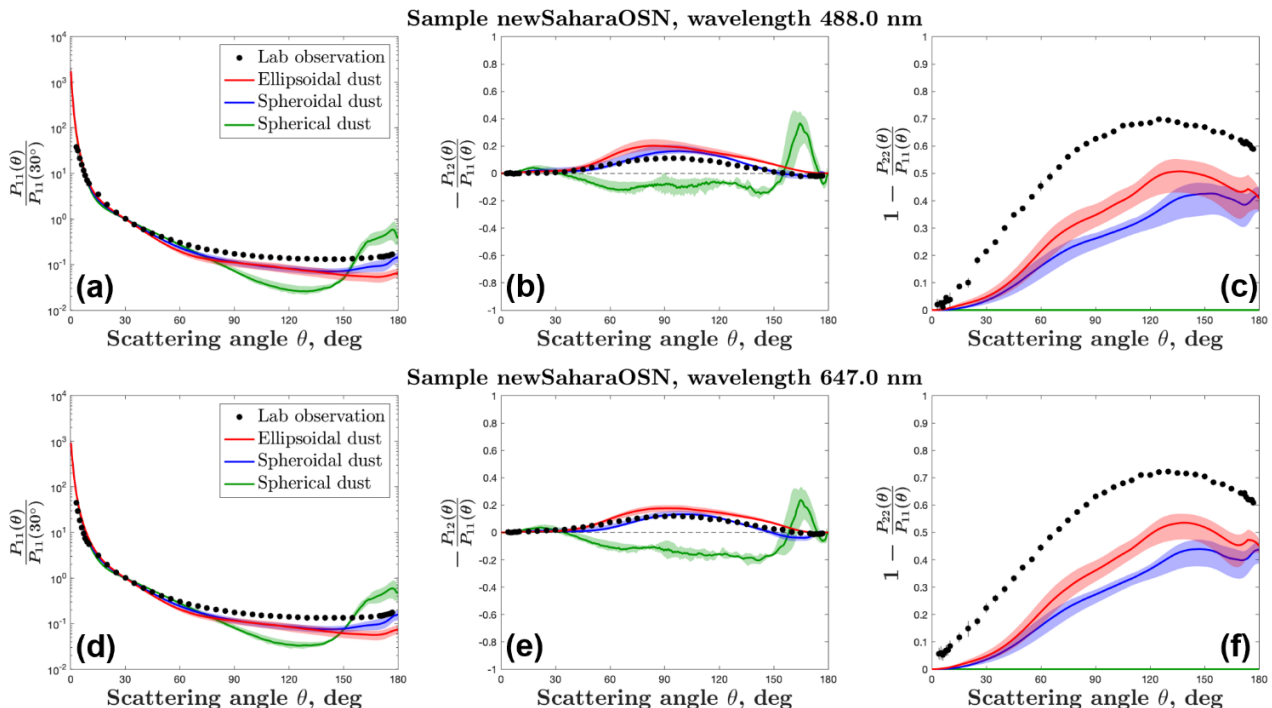


Figure 5. Same as figure 3, except for comparison of the laboratory-measured scattering matrix of AGLSD dust sample newSaharaOSN against the spherical, spheroidal, and ellipsoidal dust optics simulations at the wavelengths of 488.0 nm and 647.0 nm.

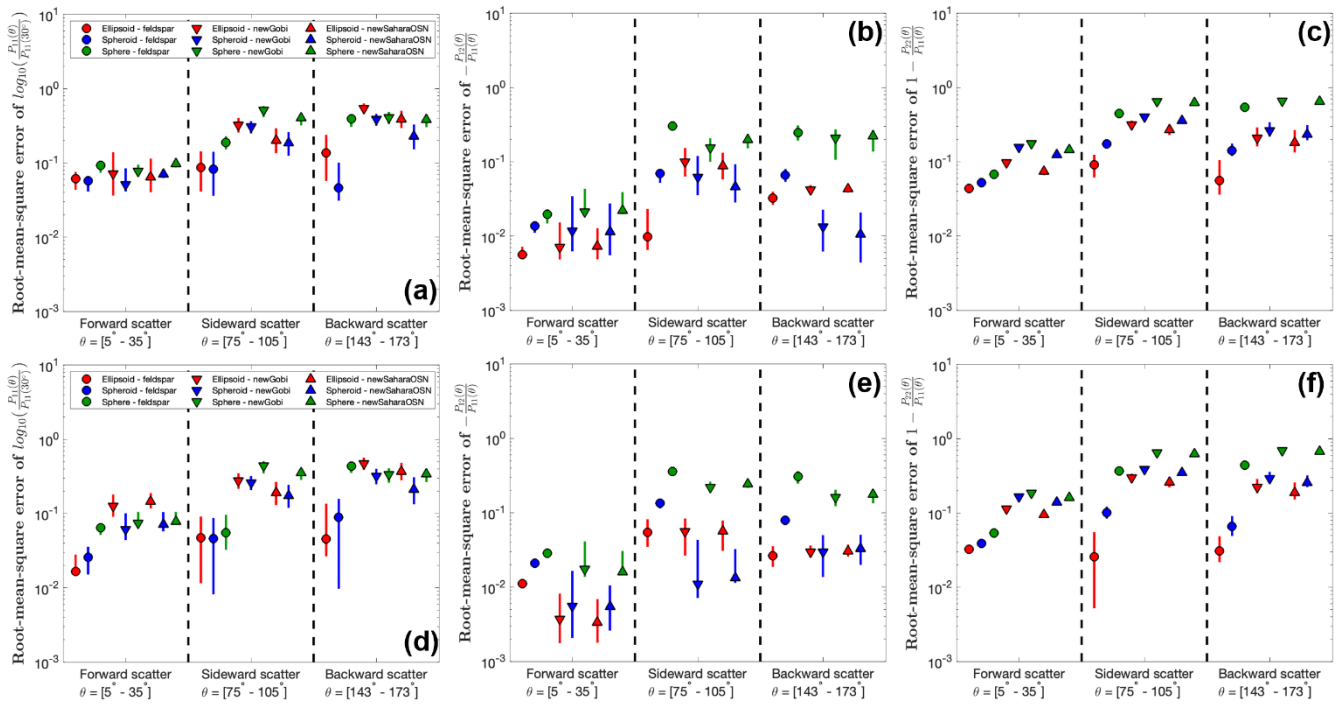


Figure 6. Root-mean-square errors (RMSEs) between the laboratory-measured and simulated scattering matrices at forward-, side-, and back-scattering angles. The top column shows RMSEs at the smaller visible wavelength, which is 441.6 nm for AGLSD mineral sample feldspar and 488.0 nm for the other two dust samples (i.e., newGobi and newSaharaOSN). The bottom column shows RMSEs at the larger visible wavelength, which is 632.8 nm for feldspar and 647.0 nm for newGobi and newSaharaOSN. The vertical error bars denote uncertainties from the dust refractive index and dust shape distributions (see Sections 2.2 and 2.3).

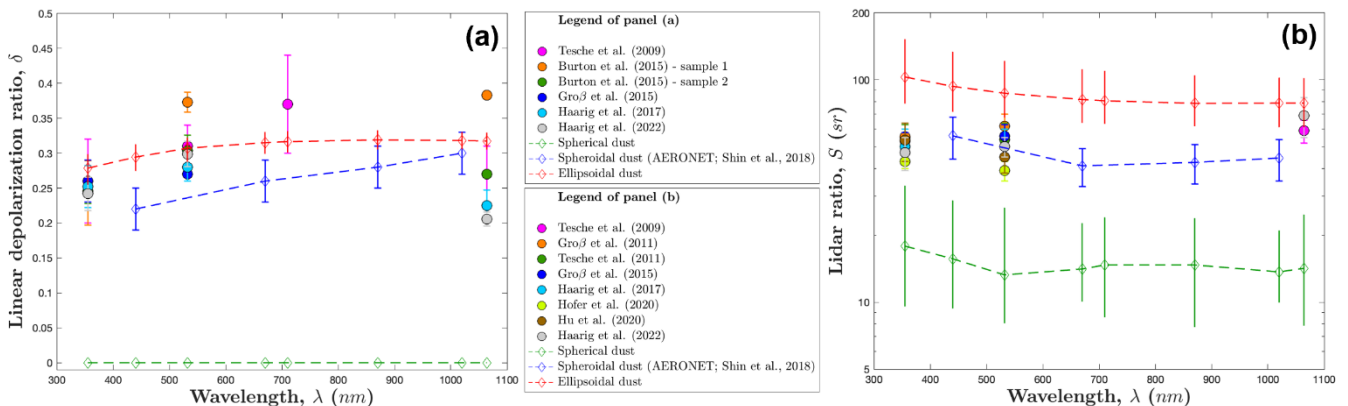


Figure 7. Comparison of the field-measured (a) linear depolarization ratio and (b) lidar ratio against the spherical, spheroidal, and ellipsoidal dust optics simulations as a function of light wavelength. In both plots, the closed markers

425 denote field lidar measurements on Saharan dust aerosols (Tesche et al., 2009; 2011; Groß et al., 2011; 2015; Burton et al., 2015; Haarig et al., 2017; 2022) and Asian dust aerosols (Hofer et al., 2020; Hu et al., 2020). For the three simulations denoted in open markers, the vertical error bars denote uncertainties from the dust refractive index and dust shape distributions (see Sections 2.2 and 2.3). The spheroidal dust optics are taken after Shin et al. (2018), who selected dust-dominated AERONET 430 observations across the globe. The results of spherical and ellipsoidal dust optics simulations are presented at both the four AERONET wavelengths and the common lidar wavelengths.

4 Discussion

We obtained new dust single-scattering properties by approximating dust as tri-axial ellipsoidal particles with observationally constrained shape distributions (Fig. 1). We find that, relative to these ellipsoidal dust optics, the spherical 435 dust optics used in most aerosol models underestimate dust extinction efficiency, mass extinction efficiency, single-scattering albedo, and asymmetry parameter for almost all dust sizes in both the shortwave and longwave spectra (Fig. 2). Furthermore, we find that the ellipsoidal dust optics can reproduce the laboratory-measured depolarization of incident polarized light (Figs. 3, 4, and 5, and 6) and the field-measured linear depolarization ratio (Fig. 7a) substantially better than the spheroidal dust 440 optics used in most retrieval algorithms. However, relative to laboratory observations, the ellipsoidal dust optics underestimate the phase function at backscattering angles by a factor of 2 (Figs. 3, 4, 5, and 6). As a result, the ellipsoidal dust optics overestimate the lidar ratio by a factor of ~ 1.3 to 2 relative to field observations (Fig. 7b). These results provide insights into several fundamental questions:

- (1) What is the implication of the missing dust asphericity in most global aerosol models?
- (2) What is the implication of the underestimated dust asphericity in most remote sensing retrieval algorithms?
- (3) How far are we from a perfect dust optical model?

4.1 Bias in global aerosol models due to missing dust asphericity

The approximation that dust aerosols are spherical, which is used in most global aerosol models (Fig. 1; Gliß et al., 450 2021), generates biases in dust single-scattering properties. Most aerosol models underestimate the four single-scattering properties (i.e., dust extinction efficiency Q_{ext} , mass extinction efficiency MEE , single-scattering albedo SSA , and asymmetry parameter g) because of the following two reasons. First, models underestimate the extinction efficiency because Q_{ext} scales with particle surface area whereas models miss the surface area enhancement due to dust asphericity. Since a spherical dust 455 particle has less surface area relative to a volume-equivalent ellipsoidal dust particle, the approximation of dust as spheres used in most models underestimates Q_{ext} . Note that our calculations neglect the dust surface roughness and sharp corners (see Section 4.3), which further increase the particle surface area, and therefore that most models possibly underestimate Q_{ext} and MEE more than our results indicate. Second, models underestimate the asymmetry parameter because an ellipsoidal dust particle scatters a larger portion of incident light in the forward direction than a volume-equivalent spherical dust particle (Nousianien and Kandler, 2015; Huang et al., 2021; Formenti et al., 2021). Since g scales with the portion of forward scattering, the spherical dust approximation used in most models underestimate g .

460 The biases in dust single-scattering properties used in most models have several key implications. First, models underestimate the mass extinction efficiency at the wavelength of 550 nm. Since many models are tuned to match the dust aerosol optical depth at 550 nm inferred from remote sensing observations (Ridley et al., 2016; Gliß et al., 2021), our finding that dust extinguishes more light per unit mass loading than models assume (Fig. 2b) indicates that models overestimate the 465 global dust mass loading. This implication is supported by a previous study (i.e., Kok et al., 2017) who found that dust asphericity can enhance dust mass extinction efficiency by $\sim 30\%$. Specifically, Kok et al. (2017) approximated dust as ellipsoidal particles with a lognormally distributed length-to-width ratio and a fixed height-to-width ratio (i.e., $HWR = 0.333$). Relative to Kok et al. (2017), our results, which account for the lognormally distributed height-to-width ratio, find an even

470 larger enhanced dust mass extinction efficiency by ~10%. This indicates that models overestimate the global dust mass loading by ~40%.

475 The second implication is that the dust single-scattering properties using observed dust shape distributions can improve estimates of dust radiative effects. For example, Ito et al. (2021) used our single-scattering properties of ellipsoidal dust aerosols to re-evaluate the dust radiative effects at the top of the atmosphere (TOA) and the surface. They integrated the Rapid Radiative Transfer Model for GCMs (RRTMG) online within the Integrated Massively Parallel Atmospheric Chemical Transport (IMPACT) model (Ito et al., 2020). They found that accounting for dust asphericity barely changes the dust radiative effect at TOA, whereas dust asphericity strongly enhances the dust cooling effect at the surface (see Table 5 of Ito et al., 2021). Specifically, at TOA, dust asphericity enhances the cooling effect in the shortwave spectrum by 0.04 W/m^2 and enhances the warming effect in the longwave spectrum by 0.04 W/m^2 , which cancels each other out. At the surface, dust asphericity enhances the cooling effect in the shortwave spectrum by 0.33 W/m^2 and enhances the warming effect in the longwave spectrum by 0.15 W/m^2 , resulting in a net cooling with a magnitude of 0.18 W/m^2 . That is, dust asphericity causes an atmospheric heating with a magnitude of 0.18 W/m^2 . Since aspherical dust has a longer lifetime than spherical dust (Huang et al., 2020; 2021), this atmospheric heating can last longer than previously thought and possibly modify regional atmospheric dynamics, especially near dust source regions.

485

4.2 Bias in remote sensing retrievals due to underestimated dust asphericity

490 Most remote sensing retrieval algorithms approximate dust aerosols as spheroidal particles with a shape distribution chosen to maximize agreement against the observed scattering matrix of AGLSD sample feldspar (Dubovik et al., 2006; Hsu et al., 2019). However, this shape distribution conflicts with observations of dust shape and substantially underestimates dust asphericity (Fig. 1). As a result, the shape approximation used in remote sensing retrievals might generate biases in the dust scattering matrix. Specifically, relative to AGLSD sample feldspar, the spheroidal dust optics, for which the shape distribution was fitted to maximize agreement with this sample, performs similarly to our ellipsoidal dust optics constrained by observed shape distributions (Figs. 3 and 6). Relative to the other two AGLSD samples (i.e., newGobi and newSaharaOSN), neither the spheroidal nor the ellipsoidal dust optics could reproduce the scattering matrix well, although the spheroidal dust optics 495 perform better in reproducing the phase function and the ellipsoidal dust optics perform better in reproducing the degree of linear polarization and the depolarization ratio (Figs. 4, 5, and 6). Drawing conclusions based on these two AGLSD samples is difficult, because the spheroidal dust optics are constrained by sample feldspar instead of these two samples, making it difficult to link the biases in optics to the problematic dust shape approximation. These findings indicate that none of the three 500 optics simulations (i.e., spherical, spheroidal, and ellipsoidal dust optics) could perfectly simulate the scattering matrix. On the one hand, the ellipsoidal dust optics could simulate the dust scattering matrix better than the spheroidal dust optics that are not constrained by the AGLSD sample feldspar. On the other hand, the ellipsoidal dust optics cannot simulate the phase function at backscattering angles well.

505 The biases in the dust scattering matrix can propagate into the depolarization ratio and lidar ratio, which are important to aerosol classification and aerosol retrieval algorithms of remote sensing products. For example, CALIOP, as the first spaceborne polarization lidar, has measured the vertical profiles of depolarization ratio and attenuated backscatter ratio across the globe since 2006 (Winker et al., 2007; 2009). CALIOP's aerosol classification algorithm first uses a threshold of attenuated 510 backscatter ratio at the wavelength of 532 nm (i.e., $> 5 \times 10^{-3}$) to mask clouds (Winker et al., 2007; Omar et al., 2009). The classification algorithm then categorizes the remaining observations with a depolarization ratio larger than 0.2 at the wavelength of 532 nm as pure dust, in between 0.075 and 0.2 over the land (ocean) as polluted dust (dusty marine), and less than 0.075 as smoke (Kim et al., 2018). As such, CALIOP's aerosol classification algorithm offers vertical profiles of each aerosol subtype. By integrating the vertical profiles of aerosol subtypes against the lidar ratio of each aerosol type, CALIOP's retrieval algorithm calculates the aerosol optical depth (AOD) at the wavelength of 532 nm. CALIOP uses a fixed value of lidar ratio for each aerosol type, specifically $44 \pm 9 \text{ sr}$ for pure dust and $55 \pm 22 \text{ sr}$ for polluted dust in its latest version 4 515 retrieval algorithm (Kim et al., 2018). The retrieved AODs by CALIOP are significantly less than coincident AOD measurements and retrievals from various spaceborne, airborne, and ground-based products (Shuster et al., 2012; Omar et al.,

2013; Kim et al., 2018). CALIOP might underestimate AOD in part because using a single value of lidar ratio and depolarization ratio remains problematic in representing the atmospheric aerosols whose microphysical properties vary spatiotemporally (Shuster et al., 2012; Kim et al., 2018).

520

The link between the lidar ratio and depolarization ratio and dust microphysical properties is also key to retrievals of dust microphysical properties. With the development of advanced lidar sensors, simultaneous observations of lidar ratio and depolarization ratio at multiple wavelengths are available (Freudenthaler et al., 2009; Tesche et al., 2009; 2011; Groß et al., 2015; Haarig et al., 2017; 2022). These datasets enable the inversion of dust microphysical properties (such as effective radius and the real and imaginary refractive index) once the look-up table on the relationship between the lidar ratio and depolarization ratio and dust microphysical properties is given (Müller et al., 2012; 2013). The look-up table of Dubovik et al. (2006) that contains spheroidal dust optics remains the most popular in the retrieval algorithms of lidar products (Müller et al., 2013; Tesche et al., 2019). The biases in the spheroidal dust optics due to underestimated dust asphericity can propagate into the aerosol classification and aerosol retrieval algorithms that further bias the estimated dust impacts.

530

Although the ellipsoidal dust optics show excellent agreement with the linear depolarization ratio (Fig. 7a), they overestimate the lidar ratio (Fig. 7b) by underestimating the backscattering intensity by a factor of ~ 2 (Figs. 3, 4, and 5). The ellipsoidal dust optics have problematic backscattering intensities because of two possible reasons. First, the computational method used by Meng et al. (2010) database to simulate ellipsoidal dust optics for particles with a size parameter $\geq \sim 10$ (see Table 2 of Meng et al., 2010), the improved geometric optics method (IGOM; Yang and Liou, 1996; 1997), underestimates the backscattering intensity by a factor of up to 2; IGOM underestimates the backscattering intensity because it ignores the coherent backscattering enhancement in the computations (Zhou and Yang, 2015; Zhou 2018; Saito et al., 2021). This indicates an inherent error in the ellipsoidal optics that is not relevant to the dust shape constraints. Ongoing work on developing IGOM backscattering correction formulas can shed light on this issue (Saito and Yang, 2022). Second, we approximate dust as smooth particles and neglect the smaller-scale surface textures such as sharp corners and surface roughness that may affect the backscattering intensity. Saito et al. (2021) approximated dust as hexahedral particles with smooth surfaces and sharp corners and found that hexahedral dust has a good agreement with field measurements of the lidar ratio. Kemppinen et al. (2015) added surface roughness to smooth particles with sharp corners and found that surface roughening can reduce the backscattering intensity. Although Kemppinen et al. (2015)'s results indicate that adding surface roughness can widen the gap between modelled and measured backscattering intensity, Kemppinen et al. (2015)'s results were based on relatively fine dust particles with a size parameter less than 10 (i.e., diameter around $1.8 \mu\text{m}$ at 550 nm wavelength). A range of studies find that dust aerosols are much coarser and can be as large as $50 \mu\text{m}$ (Kok et al., 2017; Ryder et al., 2019; Adebiyi et al., 2020; 2022). No study has been conducted to investigate the results of roughening coarse and super-coarse dust particles. As a result, it remains unclear that adding surface roughness for the ensemble of dust with various sizes will increase or decrease the gap between modelled and measured backscattering intensity. In addition, comparing the results of Saito et al. (2021) and Kemppinen et al. (2015) is difficult, because these studies are based on different dust sizes, body shapes, surface corners and edges, and levels of surface roughening. ~~and~~ ~~Therefore, it remains unknown that which factor(s) (i.e., body shape, surface corners, and surface roughness) dominates the backscattering intensity and lidar ratio.~~

545

555 4.3 Recommendations for obtaining an improved dust optical model

We developed a new dust optical model accounting for observational constraints on dust shape distributions. The newly developed ellipsoidal dust optics are in better agreement with measurements of the scattering matrix and indicate that global aerosol models underestimate the four key single-scattering properties. Although the ellipsoidal dust optics show better agreement against measurements of the depolarization ratio than the spheroidal dust optics used in most remote sensing retrievals, they overestimate the lidar ratio by a factor of ~ 2 , making these optics problematic for remote sensing products that use the backscattering signal. We make the following recommendations for developing an improved dust optical model in the future, especially for remote sensing products that use the backscattering signal.

560

565 1. We encourage more laboratory observations of the scattering matrices of atmospheric dust aerosols with simultaneous measurements of these samples' microphysical properties, namely their size distribution, refractive index, and shape distribution. The AGLSD sample feldspar had been the only dataset used in evaluating the simulated scattering matrix of dust optical models (Dubovik et al., 2006) until 2021 when two more samples (NewGobi and NewSaharaOSN) were published (Gómez Martín et al., 2021). These three samples are problematic for the following three reasons. First, their representativeness for atmospheric dust aerosols remains unknown, since the sample feldspar are not natural dust aerosols but rather was generated by grinding feldspar rocks and the two other samples are of deposited dust and are substantially coarser than is typical for atmospheric dust (Kok et al., 2017; Ryder et al., 2019; Adebiyi et al., 2020; 2022; [Liu et al., 2019; 2020](#)). Second, the refractive indices and shape distributions of the three samples were not measured simultaneously. Most studies evaluated their optical models assuming a wide range of refractive indices and particle shapes and used the averages as the evaluation results (e.g., Nousiainen and Vermeulen, 2003; Dubovik et al., 2006; Veihelmann et al., 2006; Merikallio et al., 2011; Lindqvist et al., 2014; Saito and Yang, 2021; Saito et al., 2021). Future simultaneous observations of refractive index and particle shape will help narrow the uncertainty range and identify the primary source of error. Finally, the exact backscattering and forward-scattering properties of the three samples are not available, since laboratory measurements struggle with technical difficulties at $\theta < 5^\circ$ and $\theta > 173^\circ$. Measurements at these exact scattering angles will serve as a benchmark for validating dust optical models (Miffre et al., 2016).

570

575

580

585 2. We encourage a systematic investigation of the relative impacts of dust body shape, surface corners, and surface roughness on the backscattering properties. We compared the advantages and shortcomings of the ellipsoidal dust model (the present work) and the recently-published hexahedral dust model (Saito and Yang, 2021) in Table 1. Both optical models have strong application potentials because they extensively cover wide ranges of size parameter and dust refractive index. On the one hand, the ellipsoidal dust model is more advanced than the hexahedral dust model in being constrained against measured dust shape distributions (see Section 2.2, Fig. 1, and Table 1). The hexahedral dust model is constrained against the degree of sphericity that is converted from the mean length-to-width ratio of Huang et al. (2020) and ignores the dust asphericity due to the height-to-width ratio (see Fig. 2a of Saito and Yang, 2021). As such, the hexahedral dust model underestimates the dust asphericity relative to dust shape observations. On the other hand, the hexahedral dust model is more advanced than the ellipsoidal dust model in accounting for sharp corners and coherent backscattering enhancement. The hexahedral dust model uses the physical geometric optics method (PGOM; Yang and Liou, 1996; 1997) to simulate the scattering properties for large dust particles (size parameter ≥ 50), which is more accurate than the improved geometric optics method (IGOM; Yang and Liou, 1996; 1997) used in the ellipsoidal dust model in reproducing the backscattering intensity and the lidar ratio (see the comparison between PGOM and IGOM in Fig. A1 of Saito et al., 2021). However, neither the ellipsoidal nor the hexahedral dust models can consistently reproduce the observed lidar ratio and depolarization ratio at all lidar wavelengths (Table 1). This occurs likely because neither of the two optical models accounts for the dust surface roughness, which can modify the scattering properties (Kemppinen et al., 2015; Saito et al., 2022). A future dust optical model that accounts for (1) dust body shape, (2) dust sharp corners, (3) dust surface roughness, and (4) coherent backscattering enhancement is highly encouraged.

590

595

600

605 3. Future work that defines descriptors for dust surface texture and observes the texture descriptors of atmospheric dust aerosols is needed. Although Huang et al. (2020) extensively compiled measurements of the macroscale shape characteristics of dust aerosols (i.e., dust body shape), few studies have measured the microscale shape characteristics of dust aerosols (i.e., surface corners and roughness). The two reasons that there are so few observations of the dust microscale shape are that these observations require more advanced microscopy techniques (Woodward et al., 2015) and that the descriptors to quantify the microscale shape characteristics are lacking (Nousiainen and Kandler, 2015). Advanced microscopy techniques have been used to image the microscale surface roughness of Arizona test dust less than $5 \mu\text{m}$ and ice crystals as large as $\sim 100 \mu\text{m}$; however, good descriptors are still lacking (Magee et al., 2014). These issues make it difficult to evaluate whether a dust

610

615

optical model that considers microscale shape characteristics does so in a realistic manner. Indeed, although a large number of studies have accounted for dust surface texture in developing dust optical models (e.g., Kalashnikova and Sokolik, 2004; Veihelmann et al., 2006; Gasteiger et al., 2011; Kemppinen et al., 2015; Kahnert et al., 2020), none of these shape approximations were validated against observations. The lack of good descriptors of dust surface texture thus remains a key challenge in comparing different dust optical models.

620

Table 1. A comparison between the ellipsoidal dust optical model (the present work) and the hexahedral dust optical model (Saito and Yang, 2021).

	The ellipsoidal dust optical model	The hexahedral dust optical model
Number of dust shapes considered?	121 (11 <i>LWR</i> * 11 <i>HWR</i>)	20
Constrained particle shape against observations?	Yes	Yes, but only account for <i>LWR</i> and ignore <i>HWR</i>
Considered dust body asphericity?	Yes	Yes
Considered dust sharp corners?	No	Yes
Considered dust surface roughness?	No	No
Considered coherent backscattering enhancement?	No	Yes
Consistent with observed depolarization ratio?	Yes, at all three lidar wavelengths	Yes at 532 and 1064 nm, but overestimate at 355 nm
Consistent with observed lidar ratio?	No, overestimate at all three lidar wavelengths	Yes

625

5 Conclusions

The single-scattering properties used in global aerosol models and remote sensing retrieval algorithms are critical for accurate simulations of dust distributions and dust impacts. Most global aerosol models approximate dust as spherical particles, whereas most remote sensing retrieval algorithms approximate dust as spheroidal particles with a shape distribution that conflicts with observations. These inconsistent and inaccurate shape assumptions generate biases in dust single-scattering properties.

630

Here, we obtain dust single-scattering properties by approximating dust as tri-axial ellipsoidal particles with observationally constrained shape distributions. We find that, relative to the ellipsoidal dust optics obtained here, the spherical dust optics used in most global aerosol models underestimate dust extinction efficiency, mass extinction efficiency, single-scattering albedo, and asymmetry parameter for almost all dust sizes in both the shortwave and longwave spectra. These biases in the dust optics used in global aerosol models occur because these optics neglect or underestimate the effects of dust asphericity. The ellipsoidal dust optics developed in this work – and available at <https://doi.org/10.5281/zenodo.7055766> – can be used to improve the calculation of dust radiative effects in global aerosol models.

640

We further find that our ellipsoidal dust optics show a mixed performance in reproducing angle-dependent measurements that are important for remote sensing retrievals. These optics reproduce laboratory measurements of the depolarization of incident polarized light and field measurements of the linear depolarization ratio substantially better than the spheroidal dust optics that

are used in most retrieval algorithms. However, the ellipsoidal dust optics underestimate laboratory observations of the phase function of dust at backscattering angles by a factor of ~2. As a result, these optics overestimate the lidar ratio by a factor of ~1.3 to 2 relative to field observations. Further improvements are thus needed to obtain a dust optical model that is sufficiently accurate at backscattering angles. In particular, future models should account for coherent backscattering enhancement, the macroscale shape characteristics (i.e., dust body shape), and the microscale shape characteristics (i.e., dust sharp corners and surface roughness).

Code/Data availability

The Amsterdam-Granada light scattering database is publicly available at <https://www.iaa.csic.es/scattering/> (last access: September 7th, 2022 February 6th, 2023). The spheroidal dust optics of Dubovik et al. (2006) is publicly available at <https://www.grasp-open.com/products/> after registration (last access: August 21st, 2022 February 6th, 2023). The Meng et al. (2010) database is provided by Drs. Ping Yang and Bingqi Yi upon request. Our newly developed ellipsoidal dust optics and code scripts are stored in a Zenodo data depository at <https://doi.org/10.5281/zenodo.7055766> (last access: September 7th, 2022 February 6th, 2023).

655 Author contributions

YH designed the study, analysed simulated and observational datasets, and wrote the manuscript. JFK co-designed and supervised the study. MS provided the Saito and Yang (2021) compilation on the observed lidar ratio and provided insightful discussions about the coherent backscatter enhancement and particle surface roughness. OM provided helpful guidance on the Amsterdam-Granada light scattering dataset. All authors edited and commented on the paper.

660 Competing interests

The authors declare that they have no conflict of interest.

Acknowledgments

The views and conclusions contained in this document are those of the authors and should not be interpreted as representing the official policies, either expressed or implied, of the Army Research Laboratory or the US Government. Yue Huang acknowledges support from the Columbia University Earth Institute Postdoctoral Research Fellowship (2021-2023 fellow) and the NASA grant number 80NSSC19K1346, awarded under the Future Investigators in NASA Earth and Space Science and Technology (FINESST) program. Jasper F. Kok acknowledges support by NSF grants 1552519 and 1856389, and the Army Research Office under Cooperative Agreement Number W911NF-20-2-0150. Masanori Saito acknowledges support by the Texas A&M University internal fund account 02-132503-00006. Olga Muñoz acknowledges support by grants RTI2018-095330-B-100, P18-RT-1854, and SEV-2017-0709. The authors thank Oleg Dubovik for guidance on using the Dubovik et al. (2006) kernel on the spheroidal dust optics, thank Ping Yang and Bingqi Yi for providing the Meng et al. (2010) database and interpolation code on the ellipsoidal dust optics, and thank Matthias Tesche for providing the Tesche et al. (2019) compilation on the observed linear depolarization ratio. In addition, the authors thank Timo Nousiainen, Hannakaisa Lindqvist, Adeyemi Adebiyi, Jun Meng, Pablo Saide, Marcelo Chamecki, Yoshihide Takano, Yu Gu, and the late Kuo-Nan Liou for insightful discussions.

References

Adebiyi, A. A., Kok, J. F., Murray, B. J., Ryder, C. L., Stuut, J.-B. W., Kahn, R. A., et al. (2023). A review of coarse mineral dust in the Earth system. *Aeolian Research*, 60, 100849. <https://doi.org/10.31223/X5QD36>

680 Adebiyi, A. A., & Kok, J. F. (2020). Climate models miss most of the coarse dust in the atmosphere. *Science Advances*, 6(15), eaaz9507. <https://doi.org/10.1126/sciadv.aaz9507>

Adebiyi, A. A., Kok, J. F., Wang, Y., Ito, A., Ridley, D. A., Nabat, P., & Zhao, C. (2020). Dust Constraints from joint Observational-Modelling-experiMental analysis (DustCOMM): comparison with measurements and model simulations. *Atmospheric Chemistry and Physics*, 20(2), 829–863. <https://doi.org/10.5194/acp-2019-484>

685 Ansmann, A., Seifert, P., Tesche, M., & Wandinger, U. (2012). Profiling of fine and coarse particle mass: case studies of Saharan dust and Eyjafjallajökull/Grimsvötn volcanic plumes. *Atmospheric Chemistry and Physics*, 12(20), 9399–9415. <https://doi.org/10.5194/acp-12-9399-2012>

690 Bi, L., Yang, P., Kattawar, G. W., & Kahn, R. (2010). Modeling optical properties of mineral aerosol particles by using nonsymmetric hexahedra. *Applied Optics*, 49(3), 334–342. <https://doi.org/10.1364/AO.49.000334>

Bi, L., Yang, P., Kattawar, G. W., & Kahn, R. (2009). Single-scattering properties of triaxial ellipsoidal particles for a size parameter range from the Rayleigh to geometric-optics regimes. *Applied Optics*, 48(1), 114–126. <https://doi.org/10.1364/AO.48.000114>

Bohren, C. F., & Huffman, D. R. (1983). *Absorption and scattering of light by small particles* (1st ed.). Wiley-VCH.

Burton, S. P., Hair, J. W., Kahnert, M., Ferrare, R. A., Hostetler, C. A., Cook, A. L., et al. (2015). Observations of the spectral dependence of linear particle depolarization ratio of aerosols using NASA Langley airborne High Spectral Resolution Lidar. *Atmospheric Chemistry and Physics*, 15(23), 13453–13473. <https://doi.org/10.5194/acp-15-13453-2015>

695 Colarco, P. R., Nowottnick, E. P., Randles, C. A., Yi, B., Yang, P., Kim, K.-M., et al. (2014). Impact of radiatively interactive dust aerosols in the NASA GEOS-5 climate model: Sensitivity to dust particle shape and refractive index. *Journal of Geophysical Research: Atmospheres*, 119(2), 753–786. <https://doi.org/10.1002/2013JD020046>

700 Di Biagio, C., Balkanski, Y., Albani, S., Boucher, O., & Formenti, P. (2020). Direct Radiative Effect by Mineral Dust Aerosols Constrained by New Microphysical and Spectral Optical Data. *Geophysical Research Letters*, 47(2), 1–12. <https://doi.org/10.1029/2019GL086186>

Di Biagio, C., Formenti, P., Balkanski, Y., Caponi, L., Cazaunau, M., Pangui, E., et al. (2019). Complex refractive indices and single scattering albedo of global dust aerosols in the shortwave spectrum and relationship to iron content and size. *Atmospheric Chemistry and Physics*, 19(24), 15503–15531. <https://doi.org/10.5194/acp-2019-145>

705 Di Biagio, C., Formenti, P., Balkanski, Y., Caponi, L., Cazaunau, M., Pangui, E., et al. (2017). Global scale variability of the mineral dust long-wave refractive index: a new dataset of in situ measurements for climate modeling and remote sensing. *Atmospheric Chemistry and Physics*, 17(3), 1901–1929. <https://doi.org/10.5194/acp-17-1901-2017>

Dubovik, O., Sinyuk, A., Lapyonok, T., Holben, B. N., Mishchenko, M., Yang, P., et al. (2006). Application of spheroid models to account for aerosol particle nonsphericity in remote sensing of desert dust. *Journal of Geophysical Research Atmospheres*, 111(11), D11208. <https://doi.org/10.1029/2005JD006619>

710 Formenti, P., Di Biagio, C., Huang, Y., Kok, J., Mallet, M., Boulanger, D., & Cazaunau, M. (2021). Look-up tables resolved by complex refractive index to correct particle sizes measured by common research-grade optical particle counters. *Atmospheric Measurement Techniques Discussions*, <https://doi.org/10.5194/amt-2021-403>

Formenti, P., Schütz, L., Balkanski, Y., Desboeufs, K., Ebert, M., Kandler, K., et al. (2011). Recent progress in understanding physical and chemical properties of African and Asian mineral dust. *Atmospheric Chemistry and Physics*, 11(16), 8231–8256. <https://doi.org/10.5194/acp-11-8231-2011>

715 Freudenthaler, V., Esselborn, M., Wiegner, M., Heese, B., Tesche, M., Ansmann, A., et al. (2009). Depolarization ratio profiling at several wavelengths in pure Saharan dust during SAMUM 2006. *Tellus, Series B: Chemical and Physical Meteorology*, 61(1), 165–179. <https://doi.org/10.1111/j.1600-0889.2008.00396.x>

Gasteiger, J., Wiegner, M., Groß, S., Freudenthaler, V., Toledano, C., Tesche, M., & Kandler, K. (2011). Modelling lidar-relevant optical properties of complex mineral dust aerosols. *Tellus, Series B: Chemical and Physical Meteorology*, 63(4), 725–741. <https://doi.org/10.1111/j.1600-0889.2011.00559.x>

720 Giannadaki, D., Pozzer, A., & Lelieveld, J. (2014). Modeled global effects of airborne desert dust on air quality and premature mortality. *Atmospheric Chemistry and Physics*, 14(2), 957–968. <https://doi.org/10.5194/acp-14-957-2014>

Giles, D. M., Sinyuk, A., Sorokin, M. G., Schafer, J. S., Smirnov, A., Slutsker, I., et al. (2019). Advancements in the Aerosol Robotic Network (AERONET) Version 3 database - Automated near-real-time quality control algorithm with improved cloud screening for Sun photometer aerosol optical depth (AOD) measurements. *Atmospheric Measurement Techniques*, 12(1), 169–209. <https://doi.org/10.5194/amt-12-169-2019>

725 Gliß, J., Mortier, A., Schulz, M., Andrews, E., Balkanski, Y., Bauer, S. E., et al. (2021). AeroCom phase III multi-model evaluation of the aerosol life cycle and optical properties using ground- and space-based remote sensing as well as surface in situ observations. *Atmospheric Chemistry and Physics*, 21(1), 87–128. <https://doi.org/10.5194/acp-21-87-2021>

730 Gómez Martín, J. C., Guirado, D., Frattin, E., Bermudez-Edo, M., Cariñanos Gonzalez, P., Olmo Reyes, F. J., et al. (2021). On the application of scattering matrix measurements to detection and identification of major types of airborne aerosol particles: Volcanic ash, desert dust and pollen. *Journal of Quantitative Spectroscopy and Radiative Transfer*, 271, 107761. <https://doi.org/10.1016/j.jqsrt.2021.107761>

735 González-Flórez, C., Klose, M., Alastuey, A., Dupont, S., Escribano, J., Etyemezian, V., et al. (2022). Insights into the size-resolved dust emission from field measurements in the Moroccan Sahara. *Atmospheric Chemistry and Physics Discussions*, preprint, 1–65. <https://doi.org/10.5194/acp-2022-758>

740 Grainger, R. G. (2020). Some Useful Formulae for Aerosol Size Distributions and Optical Properties. Retrieved from <http://eodg.atm.ox.ac.uk/user/grainerg/research/aerosols.pdf>

745 Groß, S., Freudenthaler, V., Schepanski, K., Toledano, C., Schäfler, A., Ansmann, A., & Weinzierl, B. (2015). Optical properties of long-range transported Saharan dust over Barbados as measured by dual-wavelength depolarization Raman lidar measurements. *Atmospheric Chemistry and Physics*, 15(19), 11067–11080. <https://doi.org/10.5194/acp-15-11067-2015>

750 Groß, S., Tesche, M., Freudenthaler, V., Toledano, C., Wiegner, M., Ansmann, A., et al. (2011). Characterization of Saharan dust, marine aerosols and mixtures of biomass-burning aerosols and dust by means of multi-wavelength depolarization and Raman lidar measurements during SAMUM 2. *Tellus, Series B: Chemical and Physical Meteorology*, 63(4), 706–724. <https://doi.org/10.1111/j.1600-0889.2011.00556.x>

755 Haarig, M., Ansmann, A., Engelmann, R., Baars, H., Althausen, D., Toledano, C., et al. (2022). First triple-wavelength lidar observations of depolarization and extinction-to-backscatter ratios of Saharan dust. *Atmospheric Chemistry and Physics*, 22(1), 355–369. <https://doi.org/https://doi.org/10.5194/acp-22-355-2022>

760 Haarig, M., Ansmann, A., Althausen, D., Klepel, A., Groß, S., Freudenthaler, V., et al. (2017). Triple-wavelength depolarization-ratio profiling of Saharan dust over Barbados during SALTRACE in 2013 and 2014. *Atmospheric Chemistry and Physics*, 17(17), 10767–10794. <https://doi.org/10.5194/acp-17-10767-2017>

765 Hofer, J., Ansmann, A., Althausen, D., Engelmann, R., Baars, H., Fomba, K. W., et al. (2020). Optical properties of Central Asian aerosol relevant for spaceborne lidar applications and aerosol typing at 355 and 532 nm. *Atmospheric Chemistry and Physics*, 20(15), 9265–9280. <https://doi.org/10.5194/acp-20-9265-2020>

770 Hovenier, J. W., van der Mee, C., & Domke, H. (2004). Transfer of Polarized Light in Planetary Atmospheres: Basic Concepts and Practical Methods (1st ed.). Springer Dordrecht. <https://doi.org/10.1007/978-1-4020-2856-4>

775 Hsu, N. C., Lee, J., Sayer, A. M., Kim, W., Bettenhausen, C., & Tsay, S.-C. (2019). VIIRS Deep Blue Aerosol Products over Land: Extending the EOS Long-Term Aerosol Data Records. *Journal of Geophysical Research: Atmospheres*, 124(7), 4026–4053. <https://doi.org/10.1029/2018jd029688>

780 Hu, Q., Wang, H., Goloub, P., Li, Z., Veselovskii, I., Podvin, T., et al. (2020). The characterization of Taklamakan dust properties using a multiwavelength Raman polarization lidar in Kashi, China. *Atmospheric Chemistry and Physics*, 20(22), 13817–13834. <https://doi.org/10.5194/acp-20-13817-2020>

785 Huang, Y., Adebiyi, A. A., Formenti, P., & Kok, J. F. (2021). Linking the different diameter types of aspherical desert dust indicates that models underestimate coarse dust emission. *Geophysical Research Letters*, 48(6), 1–12. <https://doi.org/10.1029/2020GL092054>

790 Huang, Y., Kok, J. F., Kandler, K., Lindqvist, H., Nousiainen, T., Sakai, T., et al. (2020). Climate models and remote sensing retrievals neglect substantial desert dust asphericity. *Geophysical Research Letters*, 47(6), 1–11. <https://doi.org/10.1029/2019GL086592>

Huang, Y., Kok, J. F., Martin, R. L., Swet, N., Katra, I., Gill, T. E., et al. (2019). Fine dust emissions from active sands at coastal Oceano Dunes, California. *Atmospheric Chemistry and Physics*, 19(5), 2947–2964. <https://doi.org/10.5194/acp-19-2947-2019>

Ito, A., Adebiyi, A., Huang, Y., & Kok, J. (2021). Less atmospheric radiative heating by dust due to the synergy of coarser size and aspherical shape. *Atmospheric Chemistry and Physics Discussions*, 21(22), 16869–16891. <https://doi.org/10.5194/acp-21-16869-2021>

Ito, A., Perron, M. M. G., Proemse, B. C., Strzelec, M., Gault-Ringold, M., Boyd, P. W., & Bowie, A. R. (2020). Evaluation of aerosol iron solubility over Australian coastal regions based on inverse modeling: implications of bushfires on bioaccessible iron concentrations in the Southern Hemisphere. *Progress in Earth and Planetary Science*, 7(42), 1–17. <https://doi.org/10.1186/s40645-020-00357-9>

Ito, A., Myriokefalakis, S., Kanakidou, M., Mahowald, N. M., Scanza, R. A., Hamilton, D. S., et al. (2019). Pyrogenic iron: The missing link to high iron solubility in aerosols. *Science Advances*, 5(5), eaau7671. <https://doi.org/10.1126/sciadv.aau7671>

Kahnert, M., Kanngießer, F., Järvinen, E., & Schnaiter, M. (2020). Aerosol-optics model for the backscatter depolarisation ratio of mineral dust particles. *Journal of Quantitative Spectroscopy and Radiative Transfer*, 254. <https://doi.org/10.1016/j.jqsrt.2020.107177>

Kalashnikova, O. V., & Sokolik, I. N. (2004). Modeling the radiative properties of nonspherical soil-derived mineral aerosols. *Journal of Quantitative Spectroscopy and Radiative Transfer*, 87(2), 137–166. <https://doi.org/10.1016/j.jqsrt.2003.12.026>

Kandler, K., Lieke, K., Benker, N., Emmel, C., Küpper, M., Müller-Ebert, D., et al. (2011). Electron microscopy of particles collected at Praia, Cape Verde, during the Saharan Mineral Dust Experiment: Particle chemistry, shape, mixing state and complex refractive index. *Tellus, Series B: Chemical and Physical Meteorology*, 63(4), 475–496. <https://doi.org/10.1111/j.1600-0889.2011.00550.x>

Kandler, K., Schütz, L., Deutscher, C., Ebert, M., Hofmann, H., Jäckel, S., et al. (2009). Size distribution, mass concentration, chemical and mineralogical composition and derived optical parameters of the boundary layer aerosol at Tinfou, Morocco, during SAMUM 2006. *Tellus, Series B: Chemical and Physical Meteorology*, 61(1), 32–50. <https://doi.org/10.1111/j.1600-0889.2008.00385.x>

Kandler, K., Benker, N., Bundke, U., Cuevas, E., Ebert, M., Knippertz, P., et al. (2007). Chemical composition and complex refractive index of Saharan Mineral Dust at Izaña, Tenerife (Spain) derived by electron microscopy. *Atmospheric Environment*, 41(37), 8058–8074. <https://doi.org/10.1016/j.atmosenv.2007.06.047>

Kemppinen, O., Nousiainen, T., & Lindqvist, H. (2015). The impact of surface roughness on scattering by realistically shaped wavelength-scale dust particles. *Journal of Quantitative Spectroscopy and Radiative Transfer*, 150, 55–67. <https://doi.org/10.1016/j.jqsrt.2014.05.024>

795 Kim, M.-H., Omar, A. H., Tackett, J. L., Vaughan, M. A., Winker, D. M., Trepte, C. R., et al. (2018). The CALIPSO version 4 automated aerosol classification and lidar ratio selection algorithm. *Atmospheric Measurement Techniques*, 11(11), 6107–6135. <https://doi.org/10.5194/amt-11-6107-2018>

Kiselev, A., Bachmann, F., Pedevilla, P., Cox, S. J., Michaelides, A., Gerthsen, D., & Leisner, T. (2017). Active sites in heterogeneous ice nucleation—the example of K-rich feldspars. *Science*, 355(6323), 367–371. <https://doi.org/10.1126/science.aai8034>

795 Klose, M., Jorba, O., Gonçalves Ageitos, M., Escribano, J., Dawson, M., Obiso, V., et al. (2021). Mineral dust cycle in the Multiscale Online Nonhydrostatic AtmosphRe CHEmistry model (MONARCH) Version 2.0. *Geoscientific Model Development*, 14(10), 6403–6444. <https://doi.org/10.5194/gmd-14-6403-2021>

Kok, J. F., Storelvmo, T., Karydis, V. A., Adebiyi, A. A., Mahowald, N. M., Evan, A. T., et al. (2023). Mineral dust aerosol impacts on global climate and climate change. *Nature Reviews Earth & Environment*. <https://doi.org/10.1038/s43017-022-00379-5>

800 Kok, J. F., Adebiyi, A. A., Albani, S., Balkanski, Y., Checa-Garcia, R., Chin, M., et al. (2021a). Improved representation of the global dust cycle using observational constraints on dust properties and abundance. *Atmospheric Chemistry and Physics*, 21(10), 8127–8167. <https://doi.org/10.5194/acp-21-8127-2021>

Kok, J. F., Adebiyi, A. A., Albani, S., Balkanski, Y., Checa-Garcia, R., Chin, M., et al. (2021b). Contribution of the world's main dust source regions to the global cycle of desert dust. *Atmospheric Chemistry and Physics*, 21(10), 8169–8193. <https://doi.org/10.5194/acp-21-8169-2021>

805 Kok, J. F., Ridley, D. A., Zhou, Q., Miller, R. L., Zhao, C., Heald, C. L., et al. (2017). Smaller desert dust cooling effect estimated from analysis of dust size and abundance. *Nature Geoscience*, 10, 274–278. <https://doi.org/10.1038/ngeo2912>

Kong, S., Sato, K., & Bi, L. (2022). Lidar Ratio–Depolarization Ratio Relations of Atmospheric Dust Aerosols: The Super-Spheroid Model and High Spectral Resolution Lidar Observations. *Journal of Geophysical Research: Atmospheres*, 127(4), e2021JD035629. <https://doi.org/10.1029/2021JD035629>

810 Li, L., Mahowald, N. M., Kok, J. F., Liu, X., Wu, M., Leung, D. M., et al. (2022). Importance of different parameterization changes for the updated dust cycle modelling in the Community Atmosphere Model (version 6.1). *Geoscientific Model Development*, 15(22), 8181–8219. <https://doi.org/10.5194/gmd-2022-31>

Li, L., Mahowald, N. M., Miller, R. L., Pérez Garcíá-Pando, C., Klose, M., Hamilton, D. S., et al. (2021). Quantifying the range of the dust direct radiative effect due to source mineralogy uncertainty. *Atmospheric Chemistry and Physics*, 21(5), 3973–4005. <https://doi.org/10.5194/acp-21-3973-2021>

815 Lin, W., Bi, L., Weng, F., Li, Z., & Dubovik, O. (2021). Capability of Superspheroids for Modeling PARASOL Observations Under Dusty-Sky Conditions. *Journal of Geophysical Research: Atmospheres*, 126(1), e2020JD033310. <https://doi.org/10.1029/2020JD033310>

Lindqvist, H., Jokinen, O., Kandler, K., Scheuvens, D., & Nousiainen, T. (2014). Single scattering by realistic, inhomogeneous mineral dust particles with stereogrammetric shapes. *Atmospheric Chemistry and Physics*, 14(1), 143–157. <https://doi.org/10.5194/acp-14-143-2014>

820 Liou, K.-N. (2002). An introduction to atmospheric radiation (2nd ed.). Academic Press, Inc.

Liu, J., Zhang, Q., Huo, Y., Wang, J., & Zhang, Y. (2020). An experimental study on light scattering matrices for Chinese loess dust with different particle size distributions. *Atmospheric Measurement Techniques*, 13(8), 4097–4109. <https://doi.org/10.5194/amt-13-4097-2020>

Liu, J., Zhang, Y., & Zhang, Q. (2019). Laboratory measurements of light scattering matrices for resuspended small loess dust particles at 532 nm wavelength. *Journal of Quantitative Spectroscopy and Radiative Transfer*, 229, 71–79. <https://doi.org/10.1016/j.jqsrt.2019.03.010>

825 Magee, N. B., Miller, A., Amaral, M., & Cumiskey, A. (2014). Mesoscopic surface roughness of ice crystals pervasive across a wide range of ice crystal conditions. *Atmospheric Chemistry and Physics*, 14(22), 12357–12371. <https://doi.org/10.5194/acp-14-12357-2014>

Mahowald, N. M., Ballantine, J. A., Feddema, J., & Ramankutty, N. (2007). Global trends in visibility: implications for dust sources. *Atmospheric Chemistry and Physics*, 7(12), 3309–3339. <https://doi.org/10.5194/acp-7-3309-2007>

830 Mahowald, N., Albani, S., Kok, J. F., Engelstaeder, S., Scanza, R., Ward, D. S., & Flanner, M. G. (2014). The size distribution of desert dust aerosols and its impact on the Earth system. *Aeolian Research*, 15, 53–71. <https://doi.org/10.1016/j.aeolia.2013.09.002>

Meng, Z., Yang, P., Kattawar, G. W., Bi, L., Liou, K. N., & Laszlo, I. (2010). Single-scattering properties of tri-axial ellipsoidal mineral dust aerosols: A database for application to radiative transfer calculations. *Journal of Aerosol Science*, 41(5), 501–512. <https://doi.org/10.1016/j.jaerosci.2010.02.008>

835 Meng, J., Huang, Y., Leung, D. M., Li, L., Adebiyi, A. A., Ryder, C. L., et al. (2022). Improved parameterization for the size distribution of emitted dust aerosols reduces model underestimation of super coarse dust. *Geophysical Research Letters*, 49(8), 1–12. <https://doi.org/10.1029/2021gl097287>

Merikallio, S., Lindqvist, H., Nousiainen, T., & Kahnert, M. (2011). Modelling light scattering by mineral dust using spheroids: Assessment of applicability. *Atmospheric Chemistry and Physics*, 11(11), 5347–5363. <https://doi.org/10.5194/acp-11-5347-2011>

840 Miffre, A., Mehri, T., Francis, M., & Rairoux, P. (2016). UV–VIS depolarization from Arizona test dust particles at exact backscattering angle. *Journal of Quantitative Spectroscopy and Radiative Transfer*, 169, 79–90. <https://doi.org/10.1016/j.jqsrt.2015.09.016>

Miller, R. L., Cakmur, R. V., Perlitz, J., Geogdzhayev, I. V., Ginoux, P., Koch, D., et al. (2006). Mineral dust aerosols in the NASA Goddard Institute for Space Sciences ModelE atmospheric general circulation model. *Journal of Geophysical Research Atmospheres*, 111(6), D06208. <https://doi.org/10.1029/2005JD005796>

Miller, R. L., Tegen, I., & Perlitz, J. (2004). Surface radiative forcing by soil dust aerosols and the hydrologic cycle. *Journal of Geophysical Research: Atmospheres*, 109(D4), D04203. <https://doi.org/10.1029/2003JD004085>

845 Mishchenko, M. I., & Hovenier, J. W. (1995). Depolarization of light backscattered by randomly oriented nonspherical particles. *Optics Letters*, 20(12), 1356–1358. <https://doi.org/10.1364/OL.20.001356>

Mishchenko, M. I., Travis, L. D., & Lacis, A. A. (2002). Scattering, Absorption, and Emission of Light by Small Particles. Cambridge University Press.

850 Mishchenko, M. I., & Yurkin, M. A. (2017). On the concept of random orientation in far-field electromagnetic scattering by nonspherical particles. *Optics Letters*, 42(3), 494–497. <https://doi.org/10.1364/ol.42.000494>

Müller, D., Lee, K.-H., Gasteiger, J., Tesche, M., Weinzierl, B., Kandler, K., et al. (2012). Comparison of optical and microphysical properties of pure Saharan mineral dust observed with AERONET Sun photometer, Raman lidar, and in situ instruments during SAMUM 2006. *Journal of Geophysical Research Atmospheres*, 117(D7), D07211. <https://doi.org/10.1029/2011JD016825>

855 Müller, D., Veselovskii, I., Kolgotin, A., Tesche, M., Ansmann, A., & Dubovik, O. (2013). Vertical profiles of pure dust and mixed smoke-dust plumes inferred from inversion of multiwavelength Raman/polarization lidar data and comparison to AERONET retrievals and in situ observations. *Applied Optics*, 52(14), 3178–3202. <https://doi.org/10.1364/AO.52.003178>

Muñoz, O., Moreno, F., Guirado, D., Dabrowska, D. D., Volten, H., & Hovenier, J. W. (2012). The Amsterdam-Granada Light Scattering Database. *Journal of Quantitative Spectroscopy and Radiative Transfer*, 113(7), 565–574. <https://doi.org/10.1016/j.jqsrt.2012.01.014>

860 Nousiainen, T., & Kandler, K. (2015). Light scattering by atmospheric mineral dust particles. *Light Scattering Reviews*, 9, 3–52.

Nousiainen, T., & Vermeulen, K. (2003). Comparison of measured single-scattering matrix of feldspar particles with T-matrix simulations using spheroids. *Journal of Quantitative Spectroscopy and Radiative Transfer*, 79–80, 1031–1042. [https://doi.org/10.1016/S0022-4073\(02\)00337-0](https://doi.org/10.1016/S0022-4073(02)00337-0)

865 Okada, K., Heintzenberg, J., Kai, K., & Qin, Y. (2001). Shape of atmospheric mineral particles collected in three Chinese arid-regions. *Geophysical Research Letters*, 28(16), 3123–3126. <https://doi.org/10.1029/2000GL012798>

Omar, A. H., Winker, D. M., Tackett, J. L., Giles, D. M., Kar, J., Liu, Z., et al. (2013). CALIOP and AERONET aerosol optical depth comparisons: One size fits none. *Journal of Geophysical Research Atmospheres*, 118(10), 4748–4766. <https://doi.org/10.1002/jgrd.50330>

Omar, A. H., Winker, D. M., Kittaka, C., Vaughan, M. A., Liu, Z., Hu, Y., et al. (2009). The CALIPSO automated aerosol classification and lidar ratio selection algorithm. *Journal of Atmospheric and Oceanic Technology*, 26(10), 1994–2014. <https://doi.org/10.1175/2009JTECHA1231.1>

870 Reid, E. A., Reid, J. S., Meier, M. M., Dunlap, M. R., Cliff, S. S., Broumas, A., et al. (2003). Characterization of African dust transported to Puerto Rico by individual particle and size segregated bulk analysis. *Journal of Geophysical Research*, 108(D19), 8591. <https://doi.org/10.1029/2002JD002935>

Ridley, D. A., Heald, C. L., Kok, J. F., & Zhao, C. (2016). An observationally-constrained estimate of global dust aerosol optical depth. *Atmospheric Chemistry and Physics*, 16(23), 1–31. <https://doi.org/10.5194/acp-2016-385>

875 Ryder, C. L., Highwood, E. J., Walser, A., Seibert, P., Philipp, A., & Weinzierl, B. (2019). Coarse and giant particles are ubiquitous in Saharan dust export regions and are radiatively significant over the Sahara. *Atmospheric Chemistry and Physics*, 19(24), 15353–15376. <https://doi.org/10.5194/acp-19-15353-2019>

Saito, M., & Yang, P. (2021). Advanced Bulk Optical Models Linking the Backscattering and Microphysical Properties of Mineral Dust Aerosol. *Geophysical Research Letters*, 48(17), 1–12. <https://doi.org/10.1029/2021GL095121>

880 Saito, M., Yang, P., Ding, J., & Liu, X. (2021). A comprehensive database of the optical properties of irregular aerosol particles for radiative transfer simulations. *Journal of the Atmospheric Sciences*, 78(7), 2089–2111. <https://doi.org/10.1175/jas-d-20-0338.1>

Saito, M., & Yang, P. (2022). Critical Impacts of the Small-Scale Surface Roughness of Ice Crystals on Lidar Backscattering Signals. 16th Conference on Atmospheric Radiation, Madison, WI, American Meteorological Society, Session 8.2, <https://ams.confex.com/ams/CMM2022/meetingapp.cgi/Paper/404577>.

885 Sakai, T., Nagai, T., Zaizen, Y., & Mano, Y. (2010). Backscattering linear depolarization ratio measurements of mineral, sea-salt, and ammonium sulfate particles simulated in a laboratory chamber. *Applied Optics*, 49(23), 4441. <https://doi.org/10.1364/AO.49.004441>

Scanza, R. A., Mahowald, N., Ghan, S., Zender, C. S., Kok, J. F., Liu, X., et al. (2015). Modeling dust as component minerals in the Community Atmosphere Model: Development of framework and impact on radiative forcing. *Atmospheric Chemistry and Physics*, 15(1), 537–561. <https://doi.org/10.5194/acp-15-537-2015>

890 Schuster, G. L., Vaughan, M., MacDonnell, D., Su, W., Winker, D., Dubovik, O., et al. (2012). Comparison of CALIPSO aerosol optical depth retrievals to AERONET measurements, and a climatology for the lidar ratio of dust. *Atmospheric Chemistry and Physics*, 12(16), 7431–7452. <https://doi.org/10.5194/acp-12-7431-2012>

Shin, S. K., Tesche, M., Kim, K., Kezoudi, M., Tatarov, B., Müller, D., & Noh, Y. (2018). On the spectral depolarisation and lidar ratio of mineral dust provided in the AERONET version 3 inversion product. *Atmospheric Chemistry and Physics*, 18(17), 12735–12746. <https://doi.org/10.5194/acp-18-12735-2018>

Sun, B., Yang, P., Kattawar, G. W., Zhang, X. (2017). Physical-geometric optics method for large size faceted particles. *Opt. Express*, 25, 24044–24060.

900 Swet, N., Kok, J. F., Huang, Y., Yizhaq, H., & Katra, I. (2020). Low dust generation potential from active sand grains by wind abrasion. *Journal of Geophysical Research Earth Surface*, 125(7), 1–25. <https://doi.org/10.1029/2020JF005545>

Tesche, M., Ansmann, A., Müller, D., Althausen, D., Engelmann, R., Freudenthaler, V., & Groß, S. (2009). Vertically resolved separation of dust and smoke over Cape Verde using multiwavelength Raman and polarization lidars during Saharan Mineral Dust Experiment 2008. *Journal of Geophysical Research Atmospheres*, 114(13), D13202. <https://doi.org/10.1029/2009JD011862>

905 Tesche, M., Gross, S., Ansmann, A., Müller, D., Althausen, D., Freudenthaler, V., & Esselborn, M. (2011). Profiling of Saharan dust and biomass-burning smoke with multiwavelength polarization Raman lidar at Cape Verde. *Tellus, Series B: Chemical and Physical Meteorology*, 63(4), 649–676. <https://doi.org/10.1111/j.1600-0889.2011.00548.x>

Tesche, M., Kolgotin, A., Haarig, M., Burton, S. P., Ferrare, R. A., Hostetler, C. A., & Müller, D. (2019). 3+2 + X: What is the most useful depolarization input for retrieving microphysical properties of non-spherical particles from lidar measurements using the spheroid model of Dubovik et al. (2006)? *Atmospheric Measurement Techniques*, 12(8), 4421–4437. <https://doi.org/10.5194/amt-12-4421-2019>

910 Veihelmann, B., Nousiainen, T., Kahnert, M., & van der Zande, W. J. (2006). Light scattering by small feldspar particles simulated using the Gaussian random sphere geometry. *Journal of Quantitative Spectroscopy and Radiative Transfer*, 100(1–3), 393–405. <https://doi.org/10.1016/j.jqsrt.2005.11.053>

Volten, H., Muñoz, O., Rol, E., de Haan, J. F., Vassen, W., Hovenier, J. W., et al. (2001). Scattering matrices of mineral aerosol particles at 441.6 nm and 632.8 nm. *Journal of Geophysical Research*, 106(D15), 17375–17401. <https://doi.org/10.1029/2001JD900068>

915 Winker, D. M., Hunt, W. H., & McGill, M. J. (2007). Initial performance assessment of CALIOP. *Geophysical Research Letters*, 34(19), 1–5. <https://doi.org/10.1029/2007GL030135>

Winker, D. M., Vaughan, M. A., Omar, A., Hu, Y., Powell, K. A., Liu, Z., et al. (2009). Overview of the CALIPSO mission and CALIOP data processing algorithms. *Journal of Atmospheric and Oceanic Technology*, 26(11), 2310–2323. <https://doi.org/10.1175/2009JTECHA1281.1>

920 Woodward, X., Kostinski, A., China, S., Mazzoleni, C., & Cantrell, W. (2015). Characterization of dust particles' 3D shape and roughness with nanometer resolution. *Aerosol Science and Technology*, 49(4), 229–238. <https://doi.org/10.1080/02786826.2015.1017550>

Yang, P., & Liou, K. N. (1996). Geometric-optics-integral-equation method for light scattering by nonspherical ice crystals, *Appl. Opt.*, 35, 6568–6584.

925 Yang, P., & Liou, K. N. (1997). Light scattering by hexagonal ice crystals: Solution by a ray-by-ray integration algorithm, *J. Opt. Soc. Amer. A.*, 14, 2278–2289.

Yang, P., Ding, J., Panetta, R. L., Liou, K.-N., Kattawar, G. W., & Mishchenko, M. I. (2019). On the convergence of numerical computations for both exact and approximate solutions for electromagnetic scattering by nonspherical dielectric particles, *Prog. in Electro. Res.*, 164, 27–61.

930 Yu, H., Chin, M., Yuan, T., Bian, H., Remer, L. a., Prospero, J. M., et al. (2015). The Fertilizing Role of African Dust in the Amazon Rainforest: A First Multiyear Assessment Based on CALIPSO Lidar Observations. *Geophysical Research Letters*, 42(6), 1984–1991. <https://doi.org/10.1002/2015GL063040>

Zheng, J., Zhang, Z., Garnier, A., Yu, H., Song, Q., Wang, C., et al. (2022). The thermal infrared optical depth of mineral dust retrieved from integrated CALIOP and IIR observations. *Remote Sensing of Environment*, 270, 112841. <https://doi.org/10.1016/j.rse.2021.112841>

Zhou, C., & Yang, P. (2015). Backscattering peak of ice cloud particles. *Optics Express*, 23(9), 11995–12003. <https://doi.org/10.1364/oe.23.011995>

Zhou, C. (2018). Coherent backscatter enhancement in single scattering. *Optics Express*, 26, A508–A519. <https://doi.org/10.1364/oe.26.00a508>